

Pore evolution and microstructure
during the burnout and sintering
process in BaTiO₃ based Ni-MLCCs

By

Kyung-Moo Kang

DEPARTMENT OF MATERIALS
SCIENCE AND ENGINEERING
GRADUATE SCHOOL
CHANGWON NATIONAL UNIVERSITY

Pore evolution and microstructure
during the burnout and sintering
process in BaTiO₃ based Ni-MLCCs

By

Kyung-Moo Kang

DEPARTMENT OF MATERIALS
SCIENCE AND ENGINEERING
GRADUATE SCHOOL
CHANGWON NATIONAL UNIVERSITY

Pore evolution and microstructure
during the burnout and sintering
process in BaTiO₃ based Ni-MLCCs

By

Kyung-Moo Kang

Under the Supervision of

Professor Yeon-Gil Jung

A thesis submitted to the committee of the Graduate School of
Changwon National University in partial fulfillment of the
requirements for the degree of Master of Materials Science and
Engineering

2003. 01. .

Approved by the committee of the Graduate School of Changwon
National University in partial fulfillment of the requirements for
the degree of Master of Materials Science and Engineering

Thesis committee : Tae Kwon Song _____
Bon Heun Koo _____
Yeon-Gil Jung _____

DEPARTMENT OF MATERIALS
SCIENCE AND ENGINEERING
GRADUATE SCHOOL
CHANGWON NATIONAL UNIVERSITY

Abstract

BaTiO₃ based multilayer ceramic capacitors (MLCCs) prepared by tape casting, showing X7R and Y5V characteristic, were fired with different burnout and with heating profile in the burnout and sintering processes. Also, the effects of the burnout processes and the heating profile in burnout and sintering processes, on pore structure, burnout microstructure, pore evolution in the multilayer ceramic capacitors (MLCCs) showing X7R and Y5V characteristic, were investigated to optimize the fabrication process.

In the different burnout conditions, the pore size distribution of MLCCs becomes narrower with increasing in temperature and heating rate, showing larger pore size and mono-modal pore size distribution. The cumulative pore surface area shows minimum values at higher temperature and at faster heating rate in both atmospheres. However, MLCCs of the reducing atmosphere display smaller cumulative pore surface area than that of the ambient atmosphere. The green microstructure related to the burnout process is more dependent on the burnout atmosphere and temperature than the heating rate.

MLCCs were sintered under various conditions, at heating rates of 1°C/min, 3°C/min, and 5°C/min in both processes with and without the holding time at the sintering temperature. The pore size distribution and cumulative pore surface area became broad and small, respectively, as the heating rate and sintering temperature were increased. The heating rate and the sintering temperature also affected hysteresis between the

mercury intrusion/extrusion behaviors. The microstructure revealed that the MLCCs were effectively densified in the slow heating rate, indicating that full densification would be achieved at the heating rate of 1°C/min with the holding time of 3 hours. The heating rate in the burnout process predominantly affected the pore evolution and microstructure more so than that in the sintering process, showing the effects of the holding time on removing the residual pores and on developing the final microstructure.

Contents

Abstract	i
Contents	iii
List of Tables	vi
List of Figures	vii
 Chapter 1. Introduction	 1
 Chapter 2. Research Background	 4
2.1 Definition and properties of capacitor	4
2.1.1 Definition of capacitor	4
2.1.2 History of capacitor	6
2.1.3 Element and property of capacitor	7
2.1.4 Structure and principle of capacitor	11
2.2 MLCCs (Multilayer ceramic capacitors)	14
2.2.1 Process and structure of MLCCs	14
2.2.2 Property of dielectric materials	17
2.2.3 Standard of ceramic capacitor	18
2.2.4 Temperature property of ceramic capacitor	20

**Chapter 3. Binder removal and microstructure with burnout
conditions in BaTiO₃ based Ni-MLCCs**

3.1 Introduction	23
3.2 Experimental procedure	24
3.2.1 Sample preparation	24
3.2.2 Characterization	25
3.3 Results and discussion	26
3.4 Conclusions	38

**Chapter 4. Influence of burnout process on pore structure
and burnout microstructure in BaTiO₃ based Y5V
materials**

4.1 Introduction	39
4.2 Experimental procedure	40
4.2.1 Starting materials and preparation	40
4.2.2 Characterization	41
4.3 Results and discussion	42
4.3.1 Thermal and burnout behavior	42
4.3.2 Pore size distribution and pore structure	44
4.3.3 Microstructure	46
4.4 Conclusions	57

**Chapter 5. Pore evolution and microstructure with heating
profile in BaTiO₃ based Ni-MLCCs with Y5V
specification**

5.1 Introduction	58
5.2 Experimental procedure	59
5.3 Results and discussion	61
5.4 Conclusions	73

**Chapter 6. Pore evolution and microstructural development in
Ni-MLCCs with X7R characteristic**

6.1 Introduction	74
6.2 Experimental procedure	76
6.2.1 Starting materials and preparation	76
6.2.2 Heat treatment	77
6.2.3 Characterization	78
6.3 Results and discussion	78
6.3.1 Pore evolution	78
6.3.2 Microstructural development	82
6.4 Conclusions	91

Chapter 7. Conclusions	92
-------------------------------------	-----------

Summary in Korean	94
-------------------------	----

References	95
------------------	----

List of Tables

Chapter 2. Research Background

Table 2-1. Kind of capacitors

Table 2-2. Property of capacitors

Table 2-3. Ceramic capacitors standard of JIS

Table 2-4. Standard of magnetic capacitors with EIAJ standard

Table 2-5. Assortment of CLASS I (Temperature indemnity)

Table 2-6. Assortment of CLASS II (High permittivity)

Chapter 4. Influence of burnout process on pore structure and burnout microstructure in BaTiO₃ based Y5V materials

Table 4-1. Conditions of MLCCs after burnout process in ambient atmosphere as functions of heating rate and temperature.

List of Figures

Chapter 2. Research Background

Figure. 2-1 Principle of capacitor

Figure. 2-2 Structure disc capacitor

Figure. 2-3 Flow chart for MLCCs process

Figure. 2-4 Structure of MLCCs

Figure. 2-5 Perovskite structure

Chapter 3. Binder removal and microstructure with burnout conditions in BaTiO₃ based Ni-MLCCs

Figure. 3-1 TGA/DTA curves showing weight loss and gain of MLCCs after burnout process in (A) ambient and (B) argon atmospheres.

Figure. 3-2 Conditions of MLCCs after burnout process in ambient atmosphere as functions of heating rate and temperature

Figure. 3-3 Pore size and distributions of MLCCs after burnout process at 250°C as a function of heating rate in reducing atmosphere; (A) 1°C/min, (B) 3°C/min, and (C) 5°C/min.

Figure. 3-4 Cumulative pore surface area as functions of heating rate and temperature in reducing atmosphere; (A) 200°C with (a) 1°C/min, (b) 3°C/min, (c) 5°C/min; (B) 250°C with (a) 1°C/min, (b) 3°C/min, (c) 5°C/min; (C) 300°C with (a) 1°C/min, (b) 3°C/min, (c) 5°C/min.

Figure. 3-5 Intrusion and extrusion curves of MLCCs after burnout process at 250°C as a function of heating rate in reducing atmosphere; (A) 1°C/min, (B) 3°C/min, and (C) 5°C/min.

Figure. 3-6 Fracture surface of MLCCs after burnout process at 250°C in ambient and reducing atmospheres; (A) 3°C/min in ambient atmosphere, (B) 3°C/min in reducing atmosphere, (C) 5°C/min in ambient atmosphere, and (D) 5°C/min in reducing atmosphere.

Figure. 3-7 Fracture surface of MLCCs after burnout process in reducing atmosphere; (A) 200°C with 3°C/min, (B) 300°C with 3°C/min, (C) 200°C with 5°C/min, and (D) 300°C with 5°C/min.

Chapter 4. Influence of burnout process on pore structure and burnout microstructure in BaTiO₃ based Y5V materials

Figure. 4-1 TGA/DTA curves showing weight loss and gain in

MLCCs during burnout process in ambient and argon atmospheres.

Figure. 4-2 XRD patterns for MLCCs after burnout process in ambient and reducing atmospheres at heating rate of 1°C/min: (A) ambient atmosphere with (a) 200°C, (b) 250°C, and (c) 300°C; (B) reducing atmosphere with (a) 200°C, (b) 250°C, and (c) 300°C.

Figure. 4-3 Pore size and distributions of MLCCs after burnout process in ambient atmosphere; (A) 1°C/min to 200°C, (B) 1°C/min to 250°C, (C) 1°C/min to 300°C, (D) 3°C/min to 250°C, (E) 3°C/min to 300°C, and (F) 5°C/min to 300°C.

Figure. 4-4 Pore size and distributions of MLCCs after burnout process in reducing atmosphere: (A) 1°C/min to 200°C, (B) 3°C/min to 250°C, and (C) 5°C/min to 300°C.

Figure. 4-5 Cumulative pore surface versus pore size of MLCCs after burnout process in both atmospheres; (A) ambient atmosphere with (a) 1°C/min to 200°C, (b) 3°C/min to 250°C, and (c) 5°C/min to 300°C; (B) reducing atmosphere with (a) 1°C/min to 200°C, (b) 3°C/min to 250°C, and (c) 5°C/min to 300°C.

Figure. 4-6 Intrusion-extrusion curves of MLCCs after burnout process in both atmospheres; (A) 3°C/min to 250°C in ambient atmosphere, (B) 5°C/min to 300°C in

ambient atmosphere, (C) 3°C/min to 250°C in reducing atmosphere, and (D) 5°C/min to 300°C in reducing atmosphere.

Figure. 4-7 SEM micrographs of MLCCs after burnout process in both atmospheres; (A) 1°C/min to 250°C in ambient atmosphere, (B) 1°C/min to 250°C in reducing atmosphere, (C) 5°C/min to 250°C in ambient atmosphere, (D) 5°C/min to 250°C in reducing atmosphere.

Figure. 4-8 SEM micrographs of MLCCs after burnout process as functions of heating rate and temperature in reducing atmosphere; (A) 1°C/min to 200°C, (B) 1°C/min to 300°C, (C) 5°C/min to 200°C, and (D) 5°C/min to 300°C.

Chapter 5. Pore evolution and microstructure with heating profile in BaTiO₃ based Ni-MLCCs with Y5V specification

Figure. 5-1 Schematic diagram of the heating profile at various heating rates in both processes (1°C/min, 3°C/min, and 5°C/min) and only in the sintering process (5°C/min in the burnout process).

Figure. 5-2 Pore size distributions at various heating rates and sintering temperatures: (A-1) 1°C/min to 1100°C in both

processes, (A-2) 1°C/min in the burnout process and 5°C to 1100°C in the sintering process, (B-1) 3°C/min to 1100°C in both processes, (B-2) 3°C/min to 1200°C in both processes, (C-1) 5°C/min to 1100°C in both processes, and (C-2) 5°C/min to 1200°C in both processes.

Figure. 5-3 Intrusion and extrusion behaviors of the MLCCs at various heating rates and sintering temperatures: (A-1) 1°C/min to 1100°C in both processes, (A-2) 1°C/min in the burnout process and 5°C to 1100°C in the sintering process, (B-1) 3°C/min to 1100°C in both processes, (B-2) 3°C/min to 1200°C in both processes, (C-1) 5°C/min to 1100°C in both processes, and (C-2) 5°C/min to 1200°C in both processes.

Figure. 5-4 Cumulative pore surface area as functions of heating rate and sintering temperature: (A) heating rates in both processes of (a) 1°C/min, (b) 3°C/min, and (c) 5°C/min to 1100°C and (B) sintering temperatures of (a) 1100°C and (b) 1200°C with fixed heating rates of 5°C/min and 1°C/min in burnout and sintering processes, respectively.

Figure. 5-5 Fracture micrographs of the MLCCs at different heating rates and sintering temperatures: (A-1), (B-1), and (C-1) 1100°C without holding time, (A-2), (B-2), and (C-2) 1200°C without holding time, and (A-3), (B-3), and (C-3) 1200°C with holding time of 3 hours. (A), (B), and (C)

series indicate different heating rates of 1°C/min, 3°C/min, and 5°C/min in both processes, respectively. The mark of an open circle represents a pore in the dielectric layer.

Figure. 5-6 Fracture surface of the MLCCs at different heating rates in both processes with and without holding time at 1200°C: (A-1), (B-1), and (C-1) without holding time, and (A-2) (B-2), and (C-2) with holding time of 3hours. (A) and (B) series indicate the different heating rates of 1°C/min and 3°C/min in the sintering process with a fixed heating rate of 5°C/min in the burnout process. (C) series were heat-treated at the heating rates of 1°C/min and 5°C/min in the burnout and sintering processes, respectively. The mark of an open circle represents a pore in the dielectric layer.

Chapter 6. Pore evolution and microstructural development in Ni-MLCCs with X7R characteristic

Figure. 6-1 Pore size and distributions with heating rate and sintering temperature: (A-1) 1°C/min to 1200C in both processes, (A-2) 1°C/min in burnout process and 5°C to 1300°C in sintering process, (B-1) 3°C/min to 1200C

in both processes, (B-2) 3°C/min to 1300°C in both processes, (C-1) 5°C/min to 1200°C in both processes, and (C-2) 5°C/min to 1300°C in both processes.

Figure. 6-2 Intrusion and extrusion behaviors of MLCCs with heating rate and sintering temperature: (A-1) 1°C/min to 1200°C in both processes, (A-2) 1°C/min in burnout process and 5°C to 1300°C in sintering process, (B-1) 3°C/min to 1200°C in both processes, (B-2) 3°C/min to 1300°C in both processes, (C-1) 5°C/min to 1200°C in both processes, and (C-2) 5°C/min to 1300°C in both processes.

Figure. 6-3 Cumulative pore surface area as functions of heating rate and sintering temperature: (A) changing heating rate in both processes as (a) 1°C/min, (b) 3°C/min, and (c) 5°C/min to 1200°C and (B) changing sintering temperature as (a) 1100°C and (b) 1200°C with fixed heating rates of 1°C/min in both processes.

Figure. 6-4 Fracture micrographs of MLCCs with different heating rates of (A) 1°C/min, (B) 3°C/min, and (C) 5°C/min at each sintering temperature. Numerical series of (6-1), (6-2), and (6-3) in Figs (A), (B) and (C) indicate the sintering temperature of 1200°C without holding time,

1300°C without holding time, and 1300°C with holding time of 3h, respectively.

Figure. 6-5 Fracture micrographs of MLCCs with different heating rates in both processes with and without holding time at 1300°C: (A-1) and (B-1) without holding time, and (A-2) and (B-2) with holding time of 3h. (A) series indicate the heating rates of 5°C/min and 1C/min in the burnout and sintering processes and (B) series reversed the heating rate in both processes.

Figure. 6-6 Fracture micrographs of MLCCs with the temperature of (A) 1200°C and (B) 1250°C at the heating rate of 5°C/min in both processes. Numerical series of (1) and (2) in Figs (A) and (B) indicate the holding time of 3h and 6 h, respectively.

Chapter 1. Introduction

Barium titanate (BaTiO_3) is one of the most important and widely used ceramic materials in electronics. It is mainly employed in capacitors because of its high permittivity and in thermistors with positive temperature coefficient of resistivity¹.

Barium titanate belonging to the structure of perovskite is presented polymorphs by transformation with simple displacement. The importance of these is phase transformation of cubic phase to tetragonal phase. The temperature of phase transformation of cubic structure to tetragonal phase is known as Curie temperature ($T_c=120^\circ\text{C}$). Especially the tetragonal phase has excellent dielectric properties which make it the most important compound used in the composition of ceramic capacitors, especially for the manufacture of multilayer ceramic capacitors (MLCCs)².

Multilayer ceramic capacitors (MLCCs) consist of alternately thin dielectric layers and internal electrode layers in one body, and both ends are terminated by external electrodes. The fabrication of MLCCs has been progressed to reduce the thickness of active layer, with the miniaturization in an electronic package³⁻⁵. For which the thickness of a green sheet has to be reduced with smaller particle size in starting materials. Also, the control of the heating rate in the burnout and sintering process has to be followed because the electrical properties and reliability of MLCCs are dependent on its microstructure controlled by processing techniques. Particularly, Ni electrode, which has been

used recently instead of the Ag-Pd alloys for the cost. Therefore, Ni electrode has to give more attention to the burnout process for preventing the oxidation of the electrode. Generally, to prevent the oxidation, the burnout process has been performed in a protective atmosphere using N₂ or Ar⁶⁻¹¹.

The residual pore formed after binder burnout is affected in sintering microstructure. There are many reports on the relationships between dielectric properties and microstructure, including the sintering of doped BaTiO₃ materials.⁶⁻⁹ Also, there have been numerous studies of binder-solvent systems aiming to reducing the content of binders including compaction techniques during multilayer ceramic fabrication¹²⁻¹⁴. Even few literature were found where the effect of sintering atmosphere on dielectric properties was described. However, the effects of the burnout process on pore structure and burnout microstructure of BaTiO₃ based Ni-MLCCs have not been shown in the literature, and no citation was identified where the pore evolution and microstructure were used to improve the reliability of MLCCs. Especially, influences of atmosphere, temperature, and heating rate on pore structure and burnout microstructure in the burnout process and of heating profile and holding time in the burnout and sintering processes on the pore evolution and sintering microstructure have not been revealed. Therefore, the evaluation and appreciation of pore structure, burnout microstructure, pore evolution, and sintering microstructure with burnout atmosphere, temperature, heating rate, and holding time in the burnout and sintering processes are essential for improving the electrical properties and

reliability.

In the present studies, the effects of burnout temperature, atmosphere and heating rate on pore structure and burnout microstructure have been investigated during burnout process of MLCCs. Also, the effects of heating rate and holding time on pore evolution and microstructure have been evaluated during burnout and sintering process, and the relationships among the heating rate in both processes, holding time, pore size and distribution, and microstructure were extensively discussed.

Chapter 2. Research Background

2.1 Definition and properties of capacitor

2.1.1 Definition of capacitor

A capacitor is a passive electronic component that stores energy in the form of an electrostatic field. In its simplest form, a capacitor consists of two conducting plates separated by an insulating material called the dielectric. The capacitance is directly proportional to the surface areas of the plates, and is inversely proportional to the separation between the plates. Capacitance also depends on the dielectric constant of the substance separating the plates.¹⁵

The standard unit of capacitance is the farad, abbreviated F. This is a large unit ; more common units are the microfarad, abbreviated μF ($1\mu\text{F}=10^{-6}\text{ F}$) and the picofarad, abbreviated pF ($1\text{pF}=10^{-12}\text{F}$). Capacitors can be fabricated onto integrated circuit (IC) chips. They are commonly used in conjunction with transistors in dynamic random access memory (DRAM). The capacitors help maintain the contents of memory. Because of their tiny physical size, these components have low capacitance. They must be recharged thousands of times per second or the DRAM will lose its data.¹⁵

Large capacitors are used in the power supplies of electronic

equipment of all types, including computers and their peripherals. In these systems, the capacitors smooth out the rectified utility AC, providing pure, battery-like DC.¹⁵

2.1.2 History of capacitor

The capacitor in the electric and electronic engineering is one of passive components in the circuits consisting together resistor and coil. A capacitor is an electronic component used for storing charge and energy.

In 1745 the Leyden jar, the first capacitor, was discovered by Ewald Georg von Kleist, a German inventor. A Dutch physicist Pieter van Musschenbroek of the university of Leyden also discovered the Leyden jar independently in 1746. The first Leyden jar was a glass jar partially filled with water and stoppered with a cork that had a wire inserted through the center of it that dipped into the water. The wire is brought into contact with a static electricity producer and the jar is thus charged. A conductor that comes into contact with or comes close to the wire will discharge the Leyden jar. Currently, the Leyden jar is a glass jar with a metal foil coating on the inside and the outside. A metal rod is passed through an insulating stopper in the mouth of the jar and is brought into contact with the inside foil coating. The Leyden jar is charged by charging the inside coating either positively or negatively and charging the outside coating with the opposite charge. The motive of rapidly developed capacitor became decisive climax the 2nd world war. Before, mainly natural materials were used as dielectric, the appearance of the small-sized capacitor is possible from commercial business of the metal deposition technique in Germany.¹⁶

2.1.3 Type and property of capacitor

Capacitors come in an amazing variety of shapes and size; with time, you will come to recognize their more common incarnations. the basic construction is simply two conductors near each other. For greater capacitance, you need more area and closer spacing: the usual approach is to plate some conductor onto a thin insulating material(called a dielectric), for instance, aluminized Mylar film rolled up into a small cylindrical configuration. Other popular types sre thin ceramic wafers (disc ceramics), metal foils with oxide insulators(electrolytics), and metallized mica. Each of these types has unique properties; for a brief rundown of their idiosyncrasies. The kind of capacitor was presented in Table. 2-1

Ceramic capacitors are constructed with materials such as barium titanate used as the dielectric. Internally, these capacitors are not constructed as a coil, so they can be used in high frequency applications. Typically, they are used in circuits which bypass high frequency signals to ground. These capacitors have the shape of a disk. Their capacitance is comparatively small. The aluminum electrolytic capacitors have a property of low price and high capacity. Today, the functional high molecule aluminum electrolytic capacitor and organic semiconductor capacitor is developing from the substitution of electrolysis solution. Tantalum Capacitors are electrolytic capacitors that is use a material called tantalum for the electrodes. Large values of capacitance similar to aluminum electrolytic capacitors can be obtained.

Also, tantalum capacitors are superior to aluminum electrolytic capacitors in temperature and frequency characteristics. The film capacitors take advantage of low temperature dependence. The property of capacitors is displayed in Table. 2-2¹⁷⁻¹⁹

Table 2-1. Kind of capacitors

Symbol	Sort of capacitor	Material of dielectric	Sort of electrode
CA	Aluminum solid electrolyte capacitors	Aluminum oxidation thin film	Aluminum and solid oxidation film
CC	Ceramic capacitors(sort1)	Ceramic	Metal film
CE	Aluminum solid electrolyte capacitors	Aluminum oxidation thin film	Aluminum and solid oxidation film
CF	Metalized Plastic film capacitors	Plastic film	Deposition metal film
CG	Ceramic capacitors(sort2)	Ceramic	Metal film
CK	Ceramic capacitors(sort3)	Ceramic	Metal film
CL	Tantal solid electrolyte capacitors	Tantal oxidation film	Tantal and solid electrolyte
CM	Mica capacitor	Mica	Metal film
CQ	Plastic film capacitors	Plastic film	Metal leaf
CS	Tantal solid electrolyte capacitors	Tantal oxidation film	Tantal and solid electrolyte
CU	Metalized compound film capacitors	Mixture of plastic film of variety	Deposition metal film
CW	Compound film capacitors	Mixture of plastic film of variety	Metal leaf

Table 2-2. Property of capacitors

	Film	Ceramic	Tantal	Aluminum
Dielectric	Polyester Polypropylene Polystyrene	TiO ₂ system BaTiO ₃ system PbO system	Ta ₂ O ₅ system	Al ₂ O ₃
Structure	Leaf form metal. Film form.	Disc type Barrier layer type Multilayer type	Liquid electrolytic. Solid electrolytic.	Solid electrolyte (Organic)
Rated capacity range	5pF ~ 10 μ F	0.5pF ~ 100 μ F	0.1 ~ 470 μ F	0.47 ~ 100,000 μ F
Property	Low price. Stability.	Small High reliability Low ESR Nonpolar	Small high capacity High ability. Semi-permanent.	Low price. Large capacity.
Faulty	Weak in thermal	Large temperature dependence. Large voltage dependence.	Low voltage. Polar.	Short lifetime in high temperature. Polar.

2.1.4 Structure and principle of capacitor

A capacitor consists of two identical conducting plates, which are placed in front of each other. A parallel plate capacitor consists of two conducting plates of same dimensions. These plates are placed parallel to each other. Space between the plates is filled with air or any insulating materials (dielectric). One plate is connected to positive terminal and the other is connected to negative terminal of power supply. The plate connected to positive terminal acquires positive charge and the other plate connected to negative terminal acquires equal negative charge. The charges are stored between the plates of capacitor due to attraction. The space between the plates is filled with air or any suitable dielectric material.²⁰

Disc capacitors have a single dielectric layer that limits their maximum capacitance (Fig. 2-1). This has been ameliorated in the multilayer ceramic capacitor, that is, a monolithic block of ceramic containing two sets of offset, interleaved planar electrodes. These extend to two opposite surfaces of the ceramic dielectric (Fig. 2-2). This deceptively simple structure requires a considerable amount of sophistication in material and in manufacture to produce it reliably in the quantities used in today's electronic equipment.²⁰

The development of this technology has resulted in a period of exponentially increasing use of multilayer capacitor, primarily during a period of a similar increase in the utilization of silicon-based integrated circuits. the application of these two types of devices is closely

interlinked, and the fraction of multilayer capacitors used in the United States has risen from 14% of all capacitors used in 1974 to 68% in 1984.²⁰

The principle of capacitor is based on the fact that the potential of a conductor is greatly reduced and its capacity is increased without effecting the electric charge in it by placing another earth connected conductor or an oppositely charged conductor in its neighborhood. This arrangement is therefore able to store electric charge.

Capacitors are designed to have large capacity of storing electric charge without having large dimensions.

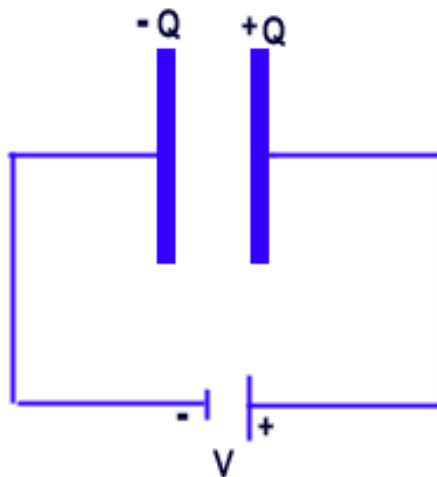


Fig. 2-1 Principle of capacitance

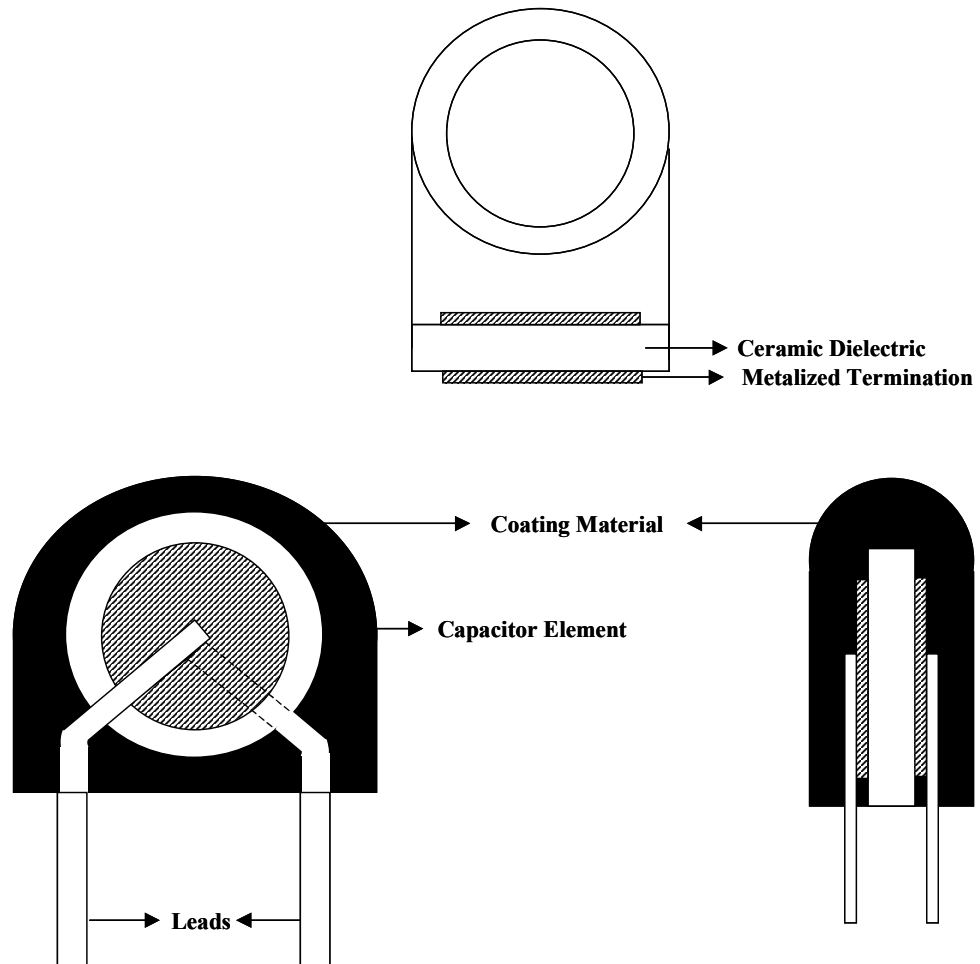


Fig. 2-2 Structure of disc capacitor

2.2 MLCCs (Multilayer ceramic capacitors)

2.2.1 Process and structure of MLCCs

Multilayer ceramic capacitors (MLCCs) are one of the most important electronic components at the surface mounting of electronic circuits. Manufacturing MLCCs is considerably more complicated than manufacturing dipped ceramic capacitors. First, the base ceramic material is mixed with a binder and is fashioned into thin sheets. Electrodes are painted onto one side of the sheets using a paint that consists of a liquid binder with fine metal particles in suspension. The metals that are used include gold, palladium, platinum, and silver alloys. The reason for using these metals is that oxygen is required for the ceramic proper to form when the base ceramic is fired. A metal such as iron would be oxidized completely during the firing process. Precious metals do not have this problem, but their cost is a major component of monolithic ceramic capacitors. However, some manufacturers have recently reported using nickel or copper for the electrodes. This promises to reduce the cost of the raw materials, but at the expense of more elaborate manufacturing processes.²¹

Once the ink is dry, the sheets are stacked on top of each other. The painted electrodes are arranged so that alternate electrodes exit from opposite ends. The top- and bottom-most layers do not have painted electrodes. The laminated layers are then compressed and fired,

which sinters them into one monolithic structure. Next, the ends are terminated, often with silver. For leaded capacitors, wires are attached, and finally the capacitor is encapsulated in plastic and marked. In the case of chip capacitors, the silver end terminations are covered with tin to aid soldering. The whole capacitor may be covered with lacquer.²¹ Figures. 2-3 and 2-4 show the detailed flowchart of the MLCCs process and structure of MLCCs.

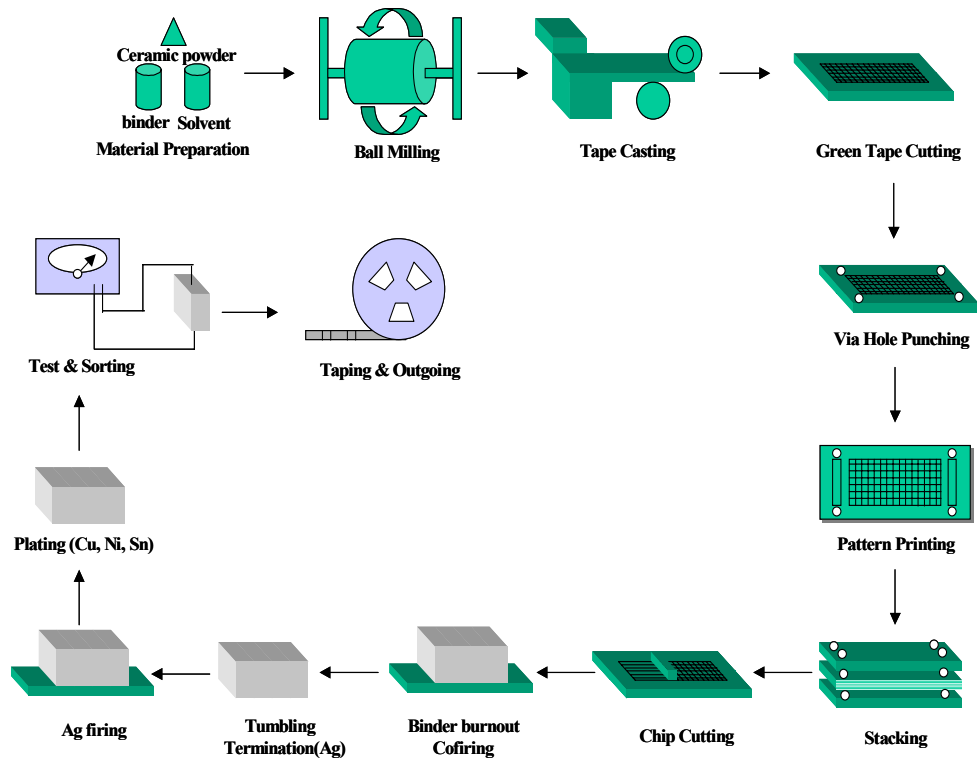


Fig. 2-3 MLCCs process

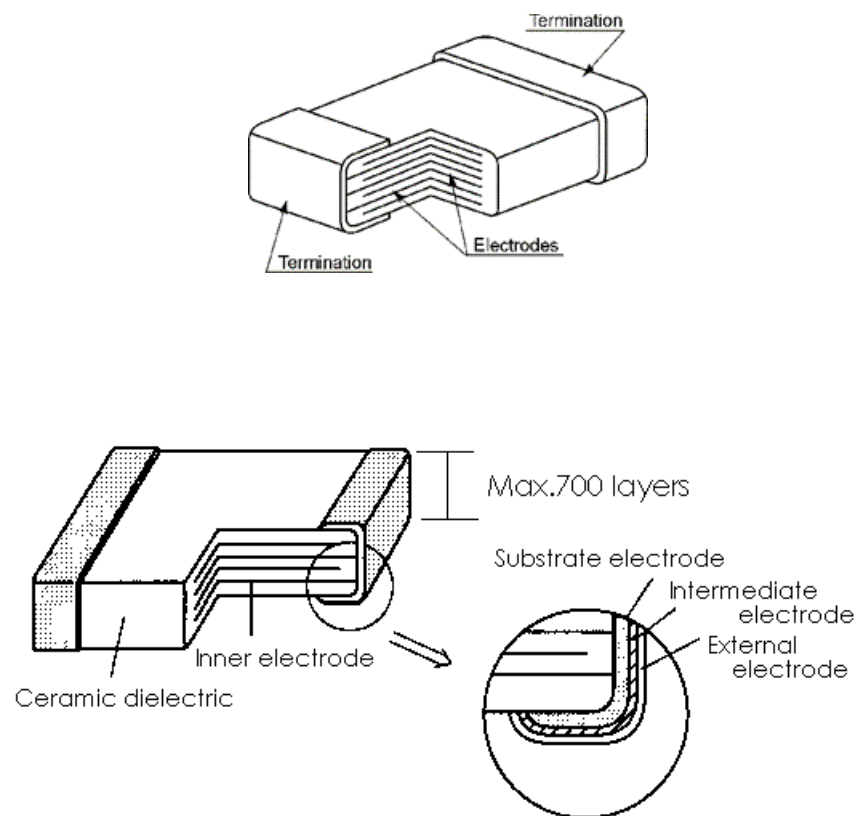


Fig. 2-4 Structure of MLCCs

2.2.2 Property of dielectric materials

The ceramic materials of dielectric materials are divided into main element of BaTiO₃ of ferroelectrics and complex perovskite materials of Pb system. The ceramic materials of high dielectric is larger the dependence of temperature and voltage.

Perovskite was named a 19th-century Russian mineralogist, Count peroski. The general formula is ABX₃: its idealized cubic structure is shown in Fig. 2-5, where the larger A cations, Ca in this case, are surrounded by 12 oxygens, and the smaller B (Ti⁴⁺)ions are coordinated by 6 oxygens.²²

BaTiO₃ has been widely used for high dielectric capacitors because of its very high dielectric constant at the Curie temperature (T_c=120°C). Some corrective modifications are required for practical application. In order to move the T_c to lower temperature, SrTiO₃, BaZrO₃ and SnTiO₃ were usually added as shifters. A number of additives have been associated with the ability to flatten the dielectric constant versus temperature characteristic of BaTiO₃. A sharp peak of the dielectric constant at the T_c can be easily flattened, and therefore, the temperature coefficient of the dielectric constant can be reduced, by adding the depressor material, such as CaTiO₃ and MgTiO₃. However, one of the most important characteristics of BaTiO₃, a very high dielectric constant at T_c should be sacrificed.²⁰

If the Curie point can be changed as a function of position by grading its composition, the transition from the ferroelectric to the

paraelectric phase would be broadened with respect to the temperature. Consequently, the temperature coefficient of the dielectric constant could be decreased.

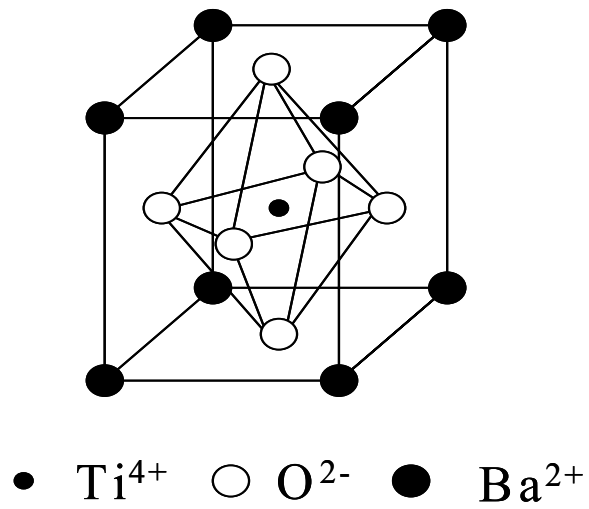


Fig. 2-5 perovskite structure

2.2.3 Standard of ceramic capacitor

The applied standard in Japan is a JIS (Japanese Industry Standard) standard. JIS is reformed to fit the international standard (IEC: International Electrotechnical Commission) with advance of skill. The standard of capacitor of JIS is presented in Table. 2-3. The examination procedure and measurement of three standard is citing in the item of JIS-C5101-10.¹⁷⁻¹⁹

Today, ceramic capacitors are not constructed as a coil, so they can be used in high frequency applications. Typically, they are used in circuits which bypass high frequency signals to ground. The classification with standard of EIAJ (Electric Industries Association Japan) is displayed in Table. 2-4. (symbol with shape, size, and property).¹⁷⁻¹⁹

Table 2-3. Ceramic capacitors standard of JIS

JIS number	Standard title	IEC standard
C5101-8	Capacitors sort (1)	60384-8
C5101-9	Capacitors sort (2)	60384-9
C5101-10	Chip capacitors	60384-10

Table 2-4. Standard of magnetic capacitors with EIAJ standard

Element	Property	Rated capacity permission limit
CC (I) Temperature indemnity	CG (0±30ppm/℃)	J (±5%) K(±10%) M(±20%) Z(+80, -20%)
	CH (0±60ppm/℃)	
	CJ (0±120ppm/℃)	
	CK (250ppm/℃)	
	SL (+350～1000ppm/℃)	
CK (II) High permittivity	Unapplied voltage 1/2 applied voltage	
	B(±10%	

2.2.4 Temperature property of ceramic capacitor

As shown in Table. 2-5, the type of Class I is characterized by small losses, high IR, high stability, linear and moderate T_C between +100 and -1500 ppm/°C with a dielectric constant between 5 and 450. The tolerances range down to $\pm 1\%$. Capacitances lower than 10 pF are difficult to produce to a percentage accuracy. The tolerances are rather stated in absolute values: ± 1 pF, ± 0.25 pF, ± 0.5 pF and ± 1 pF

Class II capacitors are characterized by high dielectric constants. The temperature dependence of the capacitance is large. Therefore EIA characterizes the ceramic with three characters that in order state the lower and the upper limit of temperature range and last capacitance change within the range. As shown in Table. 2-6, X8R specification is presenting the temperature change of rated capacity within 15% in the range of - 55°C to 150°C.¹⁷⁻¹⁹

Table 2-5. Assortment of CLASS I(Temperature indemnity)

Capacity temperature coefficient				Tolerance of temperature coefficient	
ppm/°C	Symbol	Multiplier	Symbol	ppm/°C	Symbol
		-1	0	±30	G
0.0	C	-10	1	±60	H
1.0	M	-100	2	±120	J
1.5	P	-1000	3	±250	K
2.2	R	-10000	4	±500	L
3.3	S	+1	5	±1000	M
4.7	T	+10	6	±2500	N
7.5	U	+100	7		
		+1000	8		
		+10000	9		

Table 2-6. Assortment of CLASS II (High permittivity)

Low temperature	Symbol	High temperature	Symbol	Maximum capacity change rate	Symbol
+10℃	Z	+45℃	2	±1.0%	A
-30℃	Y	+65℃	4	±1.5%	B
-55℃	X	+85℃	5	±2.2%	C
		+105℃	6	±3.3%	D
		+125℃	7	±4.7%	E
		+150℃	8	±7.5%	F
				±10.0%	P
				±15.0%	R
				±22.0%	S
				±22%, -33%	T
				±22%, -56%	U
				±22%, -82%	V

Chapter 3. Binder removal and microstructure with burnout conditions in BaTiO₃ based Ni-MLCCs

3.1. Introduction

In the fabrication process of multilayer ceramic capacitors (MLCCs), the burnout process to remove binders used for casting is one of the key processing steps. When the sufficient control in the binder burnout process is not achieved, the electrode (particularly, Ni electrode, which has been used recently to replace the Ag-Pd alloys for the cost²³) can be partially oxidized, resulting in the fatal defects in the firing process.

Therefore, to prevent the oxidation, the burnout process has been performed in a protective atmosphere using N₂ and Ar^{2,3,8-11}. Additional atmosphere control is required at all stages of the heat-treatment process, including the binder removal, sintering, and post-annealing.

For high capacitance in MLCCs, reducing of the active thickness is a much more effective strategy for increasing volume efficiency than increasing of dielectric constant alone. For this purpose, smaller size powers as the dielectric material and internal electrode need to be used, which has to give more attention to the burnout process for preventing the oxidation of the electrode and for controlling the residual carbon from the incomplete binder removal in the burnout process²⁴⁻²⁷. Also, a

pore structure formed by the binder removal and a relationship between microstructure and burnout condition are to be important for the reliability and mechanical property of MLCCs.

There are many reports on the relationships between microstructure and dielectric properties, including the sintering behavior of doped and undoped BaTiO₃ materials^{2,3,8,9}. And a few literature were found where the effect of sintering atmosphere on dielectric properties was described^{26,27}. However, the effects of burnout conditions on the binder removal and microstructure in BaTiO₃ based Ni-MLCCs, showing X7R dielectric characteristic, have not been shown in the literature.

The present work describes the influences of atmosphere, temperature, and heating rate on the binder removal and microstructure in BaTiO₃ based Ni-MLCCs. The green MLCCs were fired under different conditions as functions of atmosphere, temperature, and heating rate. The relationships among burnout conditions, pore size distribution, and microstructure have been extensively observed as well.

3.2 Experimental Procedure

3.2.1 Sample preparation

BaTiO₃ (BT-04B, Sakai Co., Japan) and Ni powder with glass frit were used as dielectric material and internal electrode. The dielectric formulation showing X7R characteristic was prepared by doping various metal oxide additives (such as Y₂O₃, MgCO₃, MnO₂, V₂O₅, Cr₂O₃) and

glass frit (Ba-Ca-Si system), totally less than 4 wt% of the formulation.

The green MLCCs were prepared by the following procedure. The powders, organic binder, dispersant, and plasticizer were mixed and dispersed in a nonaqueous media (mixture of toluene and ethanol). The green sheet with the thickness of $4\mu\text{m}$ was prepared by the so-called slot-die method (on-roll method). After the electrode was printed on the green sheet, this was then laminated and isotropic pressed, then cut to green chips. The final dimension of the green MLCCs after cutting was $4\times 2\times 2$ mm with 330 actives.

3.2.2 Characterization

Thermal behavior of the chips was analyzed by thermogravimetric analysis (TG/DTA, SDT2960, TA Instrument, U.S.A) in the ambient and argon atmospheres. The burnout atmosphere was chosen as the ambient and reducing atmospheres controlling H_2 , Ar, O_2 and H_2O . The temperature and heating rate were selected as 200°C , 250°C and 300°C , and controlled as $1^\circ\text{C}/\text{min}$ to $7^\circ\text{C}/\text{min}$ with 1°C interval, respectively, keeping the holding time at the temperature as 1 h.

Optical microscopy (EPIPHON, Nikon, Japan) was used for the investigation of the entire condition in MLCCs after the burnout process. Phase identification with the burnout atmosphere was performed by X-ray diffractometry (XRD, Rigaku Co., D/MAX-III, Japan). Pore size and distribution in MLCCs after the burnout process was measured by

porosimetry (Autoscan-25, 60, Quantachrome Corp., Syosset, NY, USA), from which the cumulative pore surface of MLCCs was compared and the pore structure was evaluated. Fracture microstructure was observed by scanning electron microscopy (SEM, S2700, Hitachi, Japan).

3.3 Results and discussion

The burnout temperature to remove the organics added could be selected as 200°C, 250°C, and 300°C based on the result of thermal analysis as shown in Fig. 3-1. Also, the information for the oxidation of the electrode could be obtained with the weight gain. In the ambient, the sudden weight loss was observed from 200°C to 400°C, and then the gain was detected to 660°C, considered as the removal of the organics and the oxidation of the electrode, respectively.

The first peak at 235°C is ascribed to the solvent and plasticizer evaporation, and the exothermic peaks at 279°C, 314°C, and 346°C are believed to be due to the decomposition of the binder (PVB)²⁸. The electrode was oxidized from 400°C and fully oxidized at 660°C in the ambient, while the argon did not reveal a sudden weight change after 300°C compared to the ambient, showing the weight loss to 500°C and then a moderate increase. The weight gain in the argon can be considered as the oxidation of the electrode due to the reaction between the activated electrode and the oxygen vaporized and/or decomposed from the organics during the heat-treatment.

MLCCs displayed a delamination after the burnout process in the

ambient as shown in Fig. 3-2. The delamination was created in the middle of MLCC from the heating rate of 7°C/min at 200°C and 6°C/min at 250°C and 300°C, showing sound condition below these conditions. Meanwhile, MLCCs prepared under the reducing ($\text{Ar}/\text{H}_2 = 97/3$) did not show any defects such as the delamination and cracks observed at the heating rate of 6°C/min and 7°C/min in the ambient. This result indicates that the higher burnout temperature needs to the slower heating rate to prevent the delamination in the burnout process of MLCCs, especially in the ambient.

In addition, because the delamination was created at the interface between the dielectric and electrode layers (even the result is not shown in this paper) and at the middle of MLCCs, the cause can be considered as following: 1) unbalance and insufficient pressing in laminating process, 2) sudden oxidation of the electrode, and 3) combustion of the binder. Even though MLCCs prepared by the reducing did not show the delamination on the outside, MLCCs with faster heating rate will give some disadvantages to the firing process, resulting in the firing defects such as inner cracks and residual stresses, etc. The effects of heating rate and temperature in the burnout process on the microstructure and residual stresses developed in the end products (MLCCs) are underway and will be reported later.

Fig. 3-3 shows the pore size distribution after the burnout process in the reducing with each heating rate at 250°C. The pore size distribution was affected by the heating rate, showing the multi-modal distribution. The mean pore size increased from $0.075\mu\text{m}$ to $0.02\mu\text{m}$ with

an increase of the heating rate from 1°C/min to 5°C/min, indicating that the results of the pore size (even the result is not shown in this paper) was dependent on the atmosphere and temperature with the smaller and larger mean pore size in the reducing and at higher temperature, respectively.

Fig. 3-4 gives the cumulative pore surface area on the pore size associated with the binder removal during the burnout process in the reducing. The cumulative pore surface area was suddenly decreased at 300°C (Fig. 3-4(C)). The cumulative pore surface area was dependent on the temperature rather than the heating rate, indicating that the full pore channel was not created until 250°C. A relatively larger pore contributed to the pore structure with an increase of temperature. The appropriate burnout condition in view of the pore size can be considered as the lower temperature and slower heating rate in the reducing. However, in views of the pore size distribution and cumulative pore surface area, the faster heating rate and higher temperature can be considered as the burnout condition.

More specifically, the form of pore channel (pore structure or pore shape) can be assumed with the hysteresis of intrusion and extrusion behaviors in mercury porosimetry. Fig. 3-5 shows the comparison between intrusion and extrusion behaviors as function of the heating rate at 250°C. The hysteresis behavior was very similar to each other except the heating rate of 5°C, even though the absolute amounts of intrusion and extrusion were different. The hysteresis decreased and the amount of mercury entrapped increased as the heating rate

increased. It is evident that the pore shape is so-called ink-bottle pores with a narrow neck and a large volume, explained by the assumption of cylindrical pores in mercury porosimetry^{29,30}. However, it can be argued that pore shape and structure will be determined by the mercury intrusion/extrusion behaviors (hysteresis behavior), because the amount of mercury retained by the sample will be influenced by a combination of at least two factors: the shape of the pores and the value of the contact angle³¹.

Many reports have been offered to account for the experimental observation that mercury extrusion curves do not overlap intrusion curves³⁰⁻³⁴. Three explanations appear to be favored by different groups in the literature: 1) the ink-bottle pore assumption²⁹⁻³¹, 2) network effects^{32,33}, and 3) a pore potential theory³³. Usually, the pores of different sizes are assumed with the same regular shape (e.g. cylinders or slits) and generally each pore is assumed to behave independently. In our study, the volume of mercury intruded was increased with an increase of the heating rate and the first pressure for intrusion was delayed with a decrease of the heating rate. These results are well consistent with the observation of the pore size distribution (Fig. 3-3) and cumulative pore surface area (Fig. 3-4(B)). Therefore, if the burnout process is performed at slower heating rate, pore structure will show narrower necks and smaller inner volume than that of faster heating rate.

The effects of the atmosphere and temperature on the microstructure related to the binder removal can be more clearly observed from the

microstructure in fracture surface (Fig. 3-6 and 3-7). The ambient (Fig. 3-6(A and C)) was more effective in removing the binder than the reducing, showing lots of the binder between particles in the reducing (Fig. 3-6(B and D)), especially in the electrode layer. However, in the ambient, the particle surface was clearer as an evidence of the binder removal, compared to the reducing. Even though the burnout process was performed in the reducing, microstructure at 300°C, as shown in Fig. 3-7 (B and D), was very similar to that at 250°C in the ambient (Fig. 3-6(A and C)) without the effect of the heating rate. If the burnout process is performed in the ambient, the binder added for the casting can be evaporated too quickly, resulting in the difference of pore structure within the chips. Also, even in the reducing, the binder can be removed suddenly at high temperature, which can also affect the green microstructure related to the rearrangement of particles during the binder removal.

Based on a result, it is possible to optimize the binder burnout condition in this system. For the binder removal and microstructure, the ambient and reducing will be proposed at the low and high temperatures, respectively, with slower heating rate.

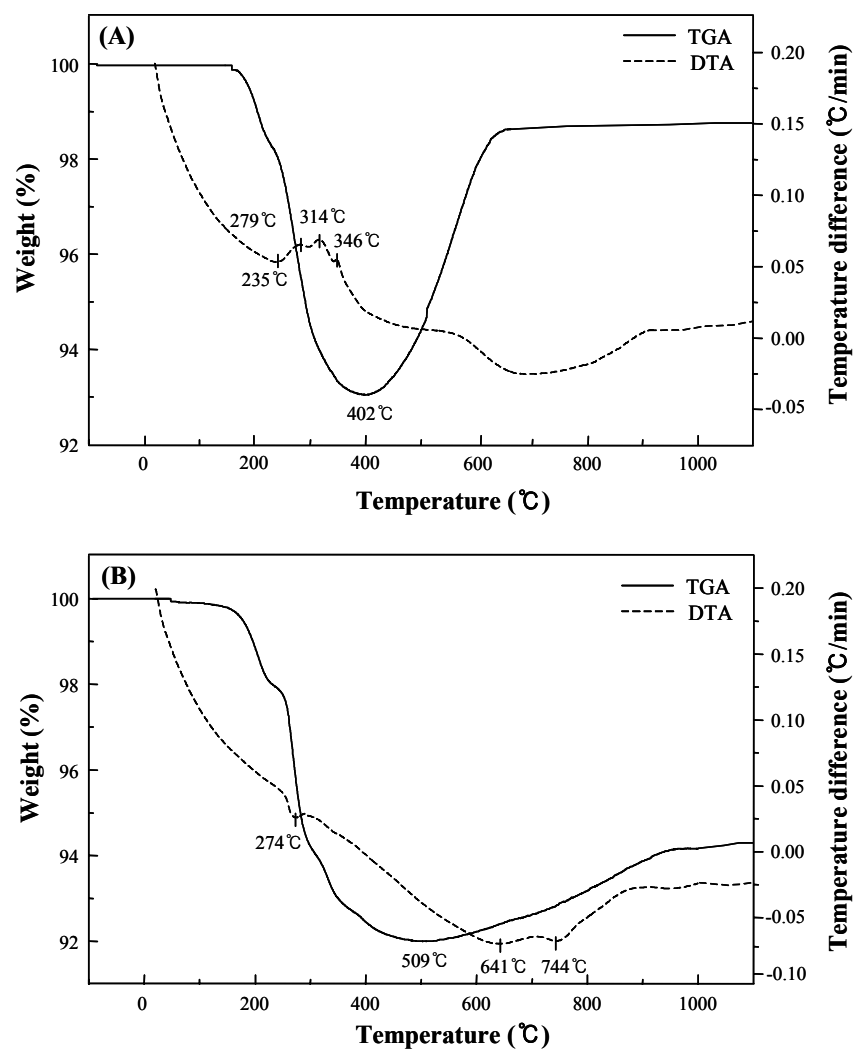


Fig. 3-1 TGA/DTA curves showing weight loss and gain of MLCCs after burnout process in (A) ambient and (B) argon atmospheres.

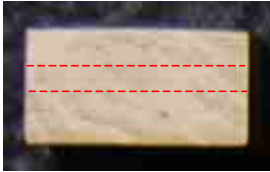

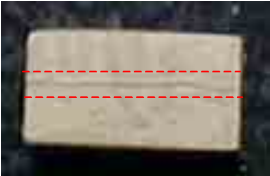

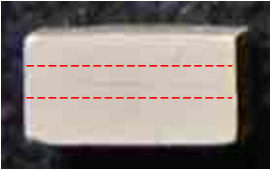
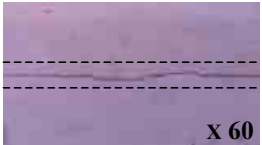
Atmosphere Condition	Ambient	
7℃/min, 200℃		
6℃/min, 250℃		
6℃/min, 300℃		

Fig. 3-2 Conditions of MLCCs after burnout process in ambient atmosphere as functions of heating rate and temperature

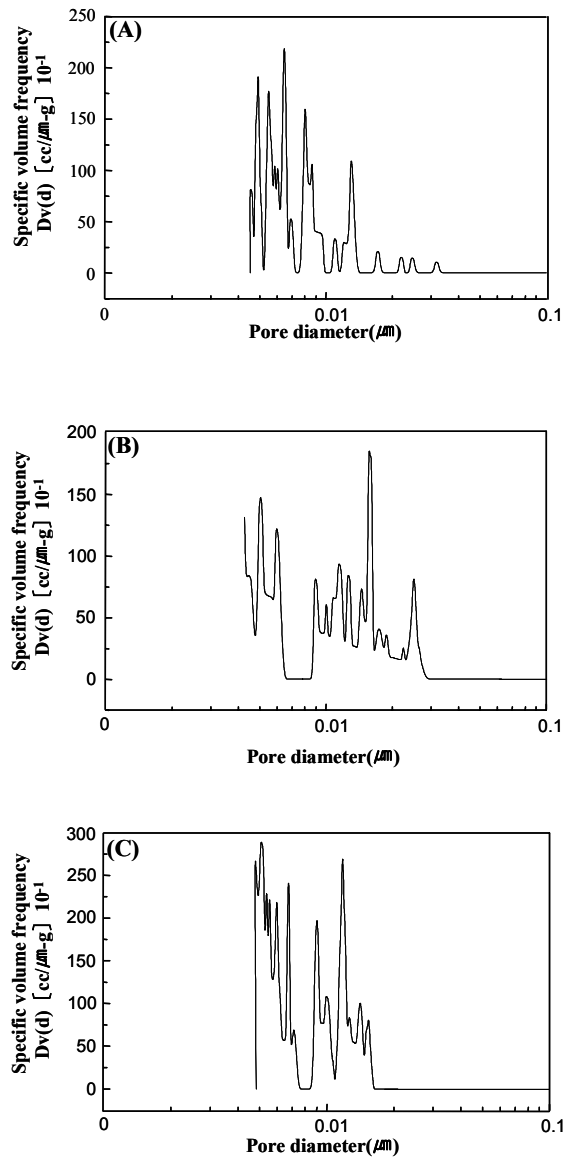


Fig. 3-3 Pore size and distributions of MLCCs after burnout at 250 °C as functions of heating rate in reducing atmosphere: (A) 1 °C/min , (B) 3 °C/min, and (C) 5 °C/min.

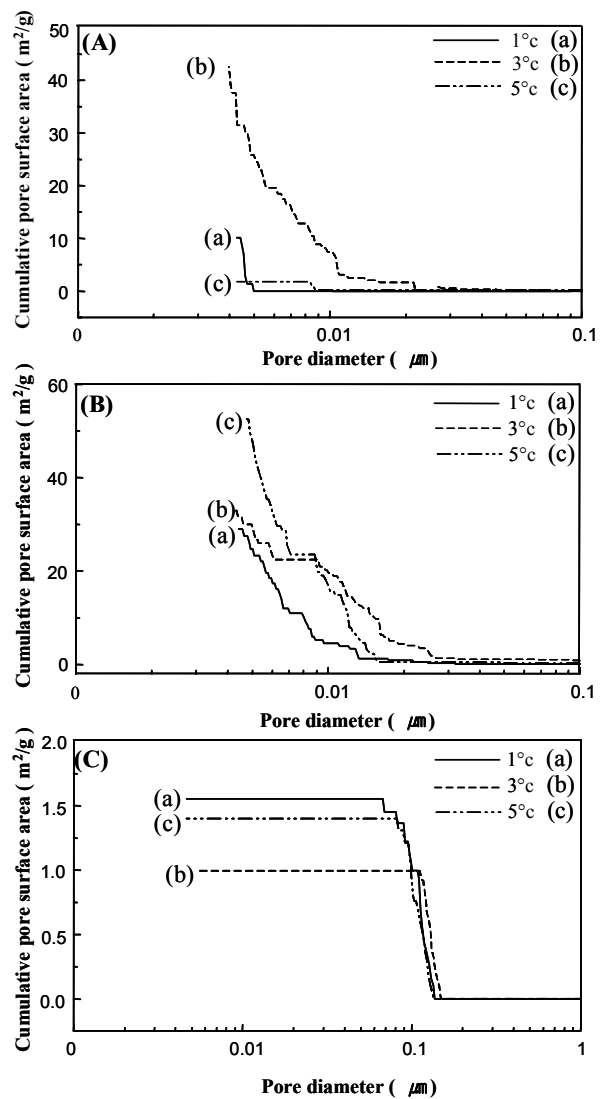


Fig. 3-4 Cumulative pore surface area as functions of heating rate and burnout temperature in reducing atmosphere: (A) 200°C with (a) 1°C/min, (b) 3°C/min, (c) 5°C/min; (B) 250°C with (a) 1°C/min, (b) 3°C/min, (c) 5°C/min; (C) 300°C with (a) 1°C/min, (b) 3°C/min, (c) 5°C/min.

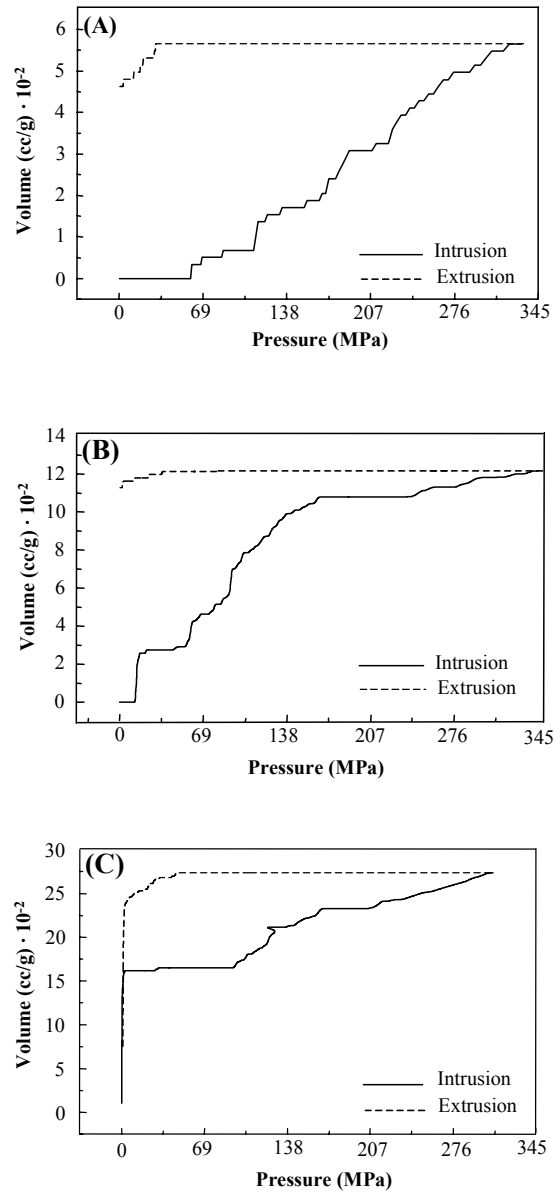


Fig. 3-5 Intrusion and extrusion curves of MLCCs after burnout at 250°C as functions of heating rate in reducing atmosphere: (A) 1°C/min , (B) 3°C/min, and (C) 5°C/min.

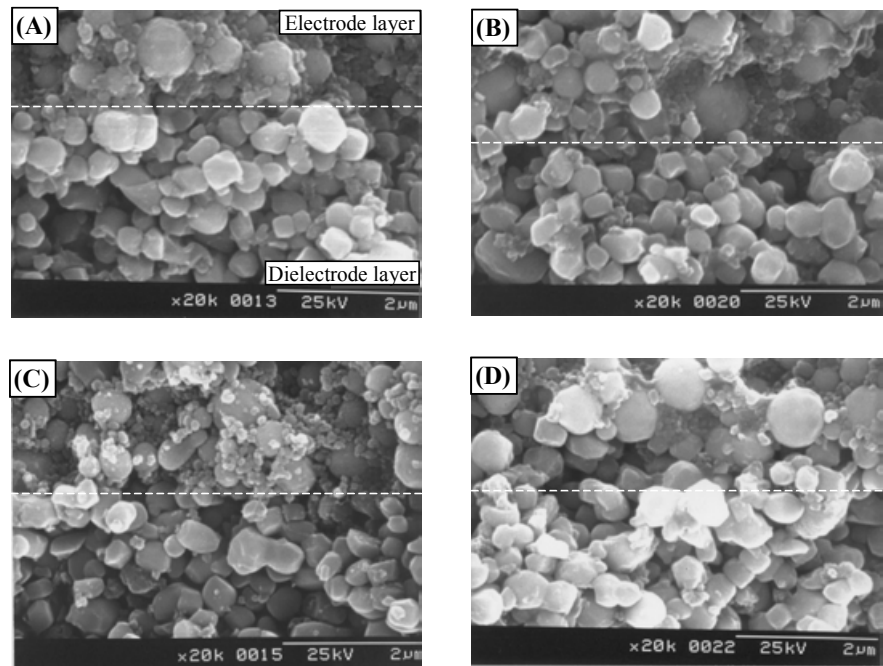


Fig. 3-6 Fracture surface of MLCCs after burnout at 250°C in ambient and reducing atmospheres: (A) 3°C/min in ambient atmosphere, (B) 3°C/min in reducing atmosphere, (C) 5°C/min in ambient atmosphere, and (D) 5°C/min in reducing atmosphere.

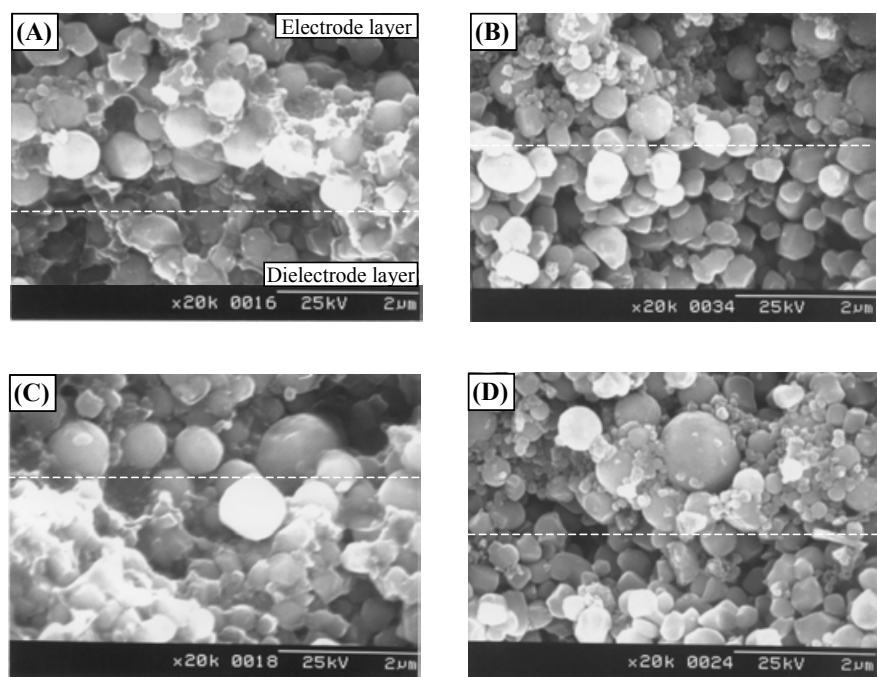


Fig 3-7 Fracture surface of MLCCs after burnout in reducing atmosphere: (A) 200°C with 3°C/min, (B) 300°C with 3°C/min, (C) 200°C with 5°C/min, and (D) 300°C with 5°C/min.

3.4 Conclusions

The effects of the burnout parameters on the binder removal and microstructure have been investigated in BaTiO₃ based Ni-MLCCs of X7R characteristic. The ambient was more effective in removing the binder than the reducing. However, the delamination was created at faster heating rate in the ambient, showing no defect even at faster heating rate and higher temperature in the reducing. The effects of the temperature and atmosphere in the burnout process on the cumulative pore surface area and microstructure are superior to the heating rate, even though the pore size distribution became narrower and the mean pore size larger with an increase of the heating rate. The burnout process has to be performed at the low temperature in the ambient and at the high temperature in the reducing with slower heating rate. Consequently, the atmosphere and temperature in the burnout process play a more important role in preventing the defects and in controlling the microstructure in MLCCs than the heating rate.

Chapter 4. Influence of burnout process on pore structure and burnout microstructure in BaTiO₃ based Y5V materials

4.1. Introduction

The technology for the fabrication of multilayer ceramic capacitors (MLCCs) has been progressed rapidly as the down sizing and cost reduction. These days, MLCCs with 3–4 μm and over 300 actives are available, and with 2–3 μm and over 600 actives are under development. For this purpose, smaller size powder and cheaper base metal (e.g., nickel; Ni) need to be used as dielectric and electrode materials, which has to give more attention to burnout process for preventing the oxidation of base metal electrode and controlling the residual carbon from organic binders^{24,35,36}. Also, a pore structure created by the burnout process and a relationship between the pore structure and the burnout process are to be important for the reliability and dielectric property of MLCCs.

There are many reports on the relationships between microstructure and dielectric properties, including the sintering of doped and undoped BaTiO₃ materials^{3,6–9}. Even few citations were found where the effect of sintering atmosphere on dielectric properties was described^{26,27}, which is related to X7R materials. The effects of the burnout process on pore

structure and burnout microstructure of BaTiO₃ based Ni-MLCCs prepared by tape casting, showing Y5V dielectric characteristics, have not appeared in the literature.

In this study, influences of burnout atmosphere, temperature, and heating rate on pore size and distribution, pore structure, and burnout microstructure of MLCCs, showing Y5V characteristic, have been investigated. The green MLCCs were fired under different conditions as function of atmosphere, heating rate, and temperature in the burnout process. Also the causes of delamination and pore formation during/after the burnout process have been discussed with oxidation, pore size and distribution, cumulative pore surface, and microstructure in MLCCs.

4.2. Experimental procedure

4.2.1. Starting Materials and Preparation

The dielectric materials employed in this work were those with an Y5V characteristic whose main composition is Ba_{0.95}Ca_{0.05}Ti_{0.82}Zr_{0.18} (Kyorix Co., Japan) + various metal oxide additives (such as Y₂O₃, MnO₂, glass frit), totaling less than 1 wt% of the formulation. Ni powder was used as internal electrode.

The green MLCCs were prepared by the following procedure. The powders, organic binder (PVB series), dispersant (RE610, Toho Chemical, Japan), and plasticizer were mixed and dispersed in a nonaqueous media (mixture of toluene and ethanol; 80:20 ratio). The

green sheet with the thickness of $9.5\mu\text{m}$ was prepared by the so-called slot-die method (on-roll method). After the electrode was printed on the green sheet, this was then laminated and isotropic pressed, and then cut to green chips. The final dimension of the green MLCCs after cutting was $4\times 2\times 2\text{ mm}$ with 150 actives.

4.2.1. Characterization

Thermal behavior of the chips was analyzed by thermogravimetric analysis (TGA/DTA, SDT2960, TA Instrument, U.S.A) in the ambient and argon atmospheres. The burnout atmosphere was chosen as the ambient and reducing atmospheres controlling H_2 , Ar, O_2 and H_2O . Temperature and heating rate were selected as 200°C , 250°C and 300°C , and controlled as $1^\circ\text{C}/\text{min}$ to $7^\circ\text{C}/\text{min}$ with 1°C interval, respectively, keeping holding time at the burnout temperature as 1h.

Optical microscopy (EPIPHON, Nikon, Japan) was used for the investigation of the entire condition in MLCCs after the burnout process. Phase identification with the burnout atmosphere was performed by X-ray diffractometry (XRD, Rigaku Co., D/MAX-III, Japan). Pore size and distribution of MLCCs after the burnout process was measured by porosimetry (Autoscan-25, 60, Quantachrome Corp., Syosset, NY, USA), from which cumulative pore surface area of MLCCs was compared^{29,30,37}. The burnout microstructure in fracture surface was observed by scanning electron microscopy (SEM, S2700, Hitachi, Japan).

4.3 Results and discussion

4.3.1 Thermal and burnout behavior

The burnout temperature to remove organic binder could be selected as 200°C, 250°C, and 300°C from the result of Fig. 4-1. Also, the weight change and the exothermic peaks in TGA/DTA curve give the information for oxidation of the electrode and for removal behavior of the binder. In the ambient atmosphere, the sudden weight loss is observed from 200°C to 380°C, and then the gain to 607°C is detected, considered as the removal of the binder and the oxidation of the electrode, respectively. The argon atmosphere also shows the weight loss to 500°C without the sudden weight change compared to the ambient atmosphere, and then the moderate increase. The exothermic peaks at 314°C and 332°C for the ambient and 311°C for the reducing are believed to be due to the oxidation of the electrode.

The weight gain in the argon atmosphere can be considered as the oxidation of the electrode due to the reaction between the activated electrode and the oxygen vaporized from the binder during the burnout process. The ambient atmosphere is effective in removing the binder at low temperature, but the oxidation of the electrode occurs from the temperature of 380°C. In contrast, the burnout process in the argon atmosphere is less effective in removing the binder, but shows a little adverse reaction at high temperature. Fig. 4-2 shows the NiO peaks detected in both atmospheres as evidence of the oxidation. Even the

burnout process is performed in the reducing atmosphere, the NiO peak appears at all temperatures because oxygen can be adsorbed on Ni powder during powder processing and the oxidation can be associated with the binder removal during the burnout process.

MLCCs after the burnout process display a delamination in the ambient atmosphere as shown in table 4-1. The delamination is created in the middle of MLCCs from the heating rate of 7°C/min to 200°C, and 6°C/min to 250°C and 300°C, showing sound condition below this heating rate. Meanwhile, MLCCs prepared under the reducing atmosphere (Ar/H₂ = 97/3) do not present any defects—such as the delamination and crack observed in the ambient atmosphere to the heating rate of 7°C/min. These phenomena are strongly dependent on temperature and heating rate even though they will also be dependent on the composition of MLCCs, indicating that the higher burnout temperature needs to the slower heating rate to prevent the delamination in MLCCs after the burnout process. In addition, because the delamination is created at the interface between electrode and active layers and at the middle of MLCCs, the cause of the delamination can be considered as following^{24,35,38-42}: 1) unbalance and insufficient pressing in laminating, 2) sudden oxidation of the electrode, and 3) combustion of the binder. Even MLCCs prepared by the reducing atmosphere do not show the delamination on the outside, MLCCs with faster heating rate in the burnout process will give some disadvantage to the firing process, resulting in firing defects such as inner cracks and residual stresses, *etc.*^{26,43}. The effects of heating rate and temperature on microstructure

and residual stresses developed in the end-products (MLCCs) are underway and will be reported later.

4.3.2 Pore size distribution and pore structure

Fig. 4-3 shows the pore size distribution of MLCCs after the burnout process in the ambient atmosphere. The pore size distribution becomes narrower with an increase of temperature, showing bi-modal distribution in Fig. 4-3(C); even the mean pore size becomes larger. When heating rate is increased, the bi-modal distribution becomes mono-modal distribution. The mean pore size is also increased with an increase of heating rate. Also, in the reducing atmosphere (Fig. 4-4), the pore size distribution becomes narrower with increases in temperature and heating rate, showing mono-modal distribution at the temperature of 300°C and the heating rate of 5°C/min. As a result, the burnout temperature and heating rate preferentially influence on the pore size distribution and the mean pore size, respectively.

The effects of temperature and heating rate on pore formation during/after burnout process are more clearly observed in cumulative pore surface as shown in Fig. 4-5. Even though the large pore creates in higher temperature and faster heating rate, the cumulative pore surface area associated with the binder removal during the burnout process shows the minimum values in higher temperature and faster heating rate, independence of the atmosphere. This means that the pore size is increased and the pore volume is decreased with increases in

temperature and heating rate. While MLCCs of the reducing atmosphere display smaller cumulative pore surface area than that of the ambient atmosphere, which are allowed to the burnout process in the reducing atmosphere as the temperature of 300°C and the heating rate of 5°C/min. However, the other factors in the burnout process such as the binder removal and burnout microstructure have to be considered.

More specially, the form of pore channel (pore structure or pore shape) can be assumed with the hysteresis of intrusion/extrusion behavior in mercury porosimetry. Fig. 4-6 shows the comparison between intrusion/extrusion behaviors in MLCCs after the burnout process with the ambient and reducing atmospheres. The hysteresis behavior is dependent on the mean pore size and pore size distribution, even the absolutely amounts of intrusion/extrusion are different. After the burnout process at 250°C with 3°C/min in the ambient atmosphere, almost 85% of the total mercury intruded remains in MLCCs. It is evident that mercury penetrated into so-called ink-bottle pores, explained by the assumption of cylindrical pores in mercury porosimetry^{38,39}, will not leave these pores through the smaller pore entrance during extrusion. However, in the other hysteresis, the extrusion starts to take place at much higher pressure. It means that the pore structure is open with each other and the pore shape is the ink-bottle pore with a broad neck. However, it can be argued that pore shape and structure will be determined by the mercury intrusion/extrusion behavior (hysteresis behavior) because the amount of mercury retained by the sample will be influenced by a combination of at least two factors: the shape of the

pores and the value of the contact angle.³¹

Many reports have been offered to account for the experimental observation that mercury extrusion curves do not overlap intrusion curves^{29,30,32-34}. Three explanations appear to be favored by different groups in the literature: 1) the ink-bottle pore assumption^{29,30}, 2) network effects^{32,33}, and 3) a pore potential theory³⁴. Usually, the pores of different size are assumed to be all of the same regular shape (e.g. cylinders or slits) and generally each pore is assumed to behave independently. In our system, the volume of mercury intruded is decreased with increases in temperature and heating rate. These results are well consistent with the observation of the pore size and distribution. Therefore, if the burnout process is performed at lower temperature and slower heating rate, pore structure will show narrower neck and larger inner volume than that of higher temperature and faster heating rate.

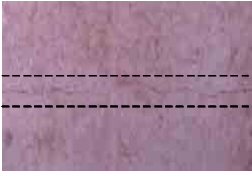
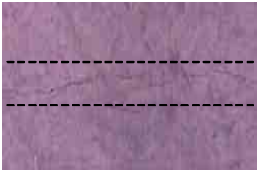
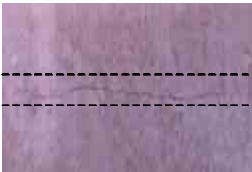
4.3.3 Microstructure

The effects of heating rate, atmosphere, and temperature on the burnout microstructure can be clarified from Figs. 4-7 and 4-8. The ambient atmosphere is more effective to remove the binder than the reducing atmosphere, showing lots of the binder between particles in the reducing atmosphere. While, in the ambient atmosphere, the particle surface is clearer compared to the reducing atmosphere as the evidence of combustion. However, the effect of heating rate on the burnout

microstructure is not observed in both atmospheres. As temperature is increased in the reducing atmosphere, the interface of particles is cleared as shown in Fig. 4-8, showing the similar microstructure with the ambient atmosphere. Therefore, if the burnout process is performed in the ambient atmosphere, the binder can be evaporated too quickly, resulting in the difference of pore structure within the chips. However, even in the reducing atmosphere, faster heating rate can remove the binder suddenly, which can also affect the degree of densification in the sintered bodies.

As a result, the optimum burnout condition in this system is the temperature of 300°C, the heating rate of 1°C/min, and the reducing atmosphere in the view of the cumulative pore surface area and microstructure related to the binder removal.

Table 4-1. Conditions of MLCCs after burnout process in ambient atmosphere as functions of heating rate and temperature.

<div> <div>Atmosphere</div> <div>Ambient</div> </div> <div>Condition</div>	
200℃, 7℃/min	
250℃, 6℃/min	
300℃, 6℃/min	

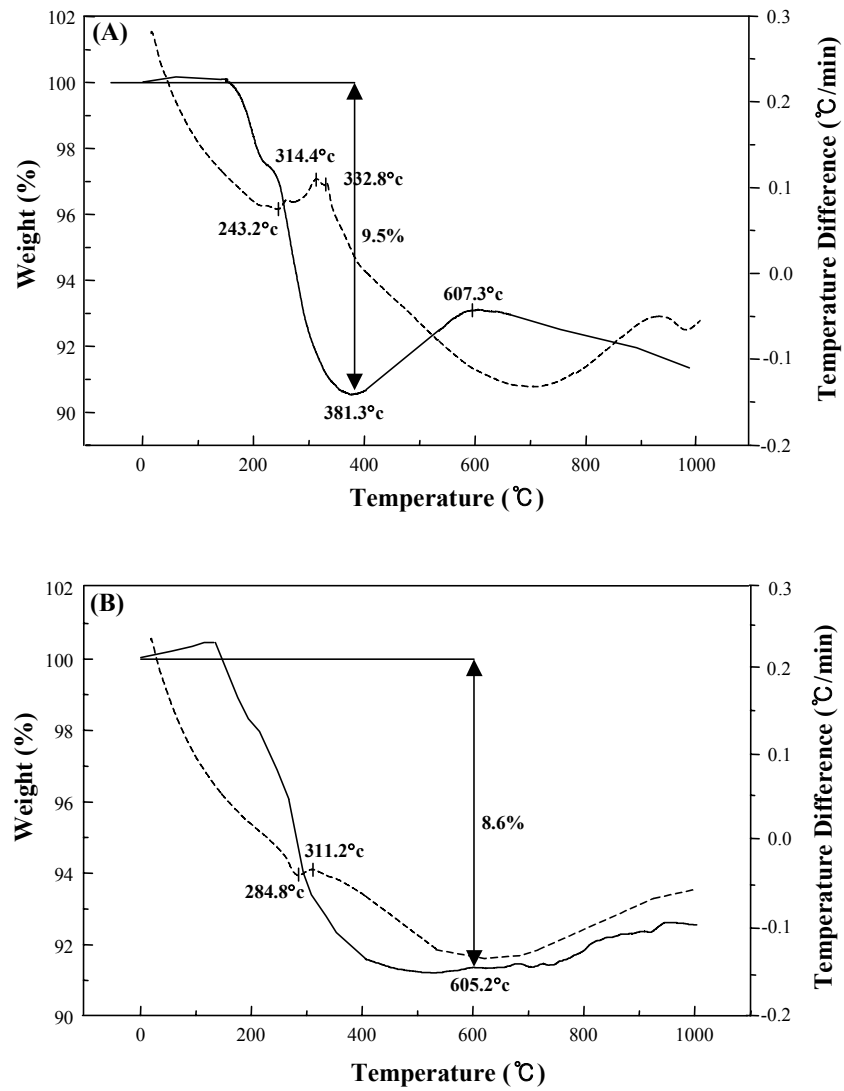


Fig. 4-1 TGA/DTA curves showing weight loss and gain in MLCCs during burnout process in ambient and argon atmospheres.

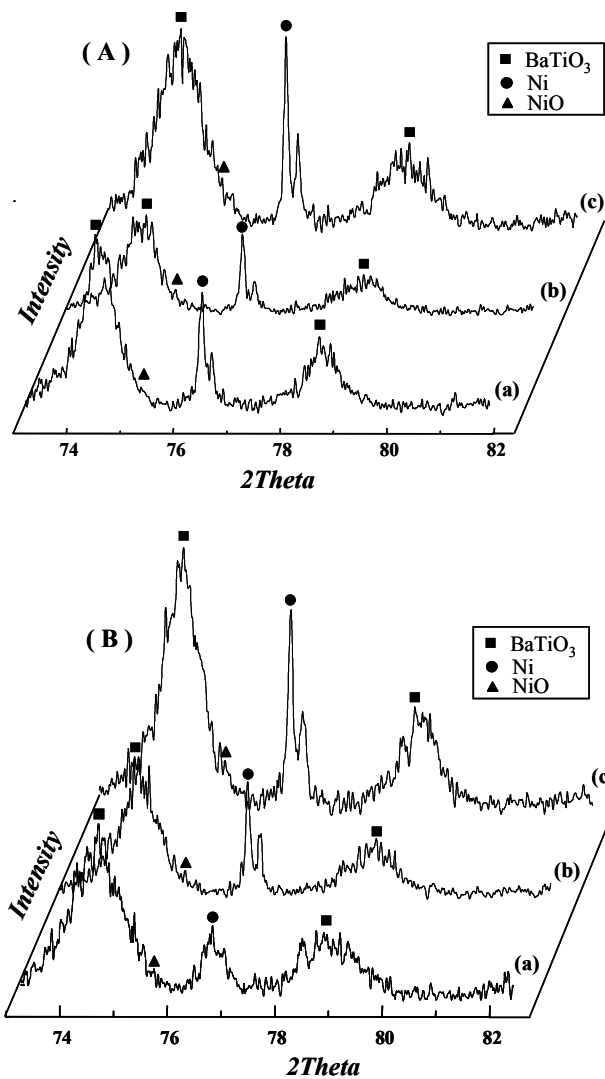


Fig. 4-2 XRD patterns for MLCCs after burnout process in ambient and reducing atmospheres at heating rate of 1°C/min: (A) ambient atmosphere with (a) 200°C, (b) 250°C, and (c) 300°C; (B) reducing atmosphere with (a) 200°C, (b) 250°C, and (c) 300°C.

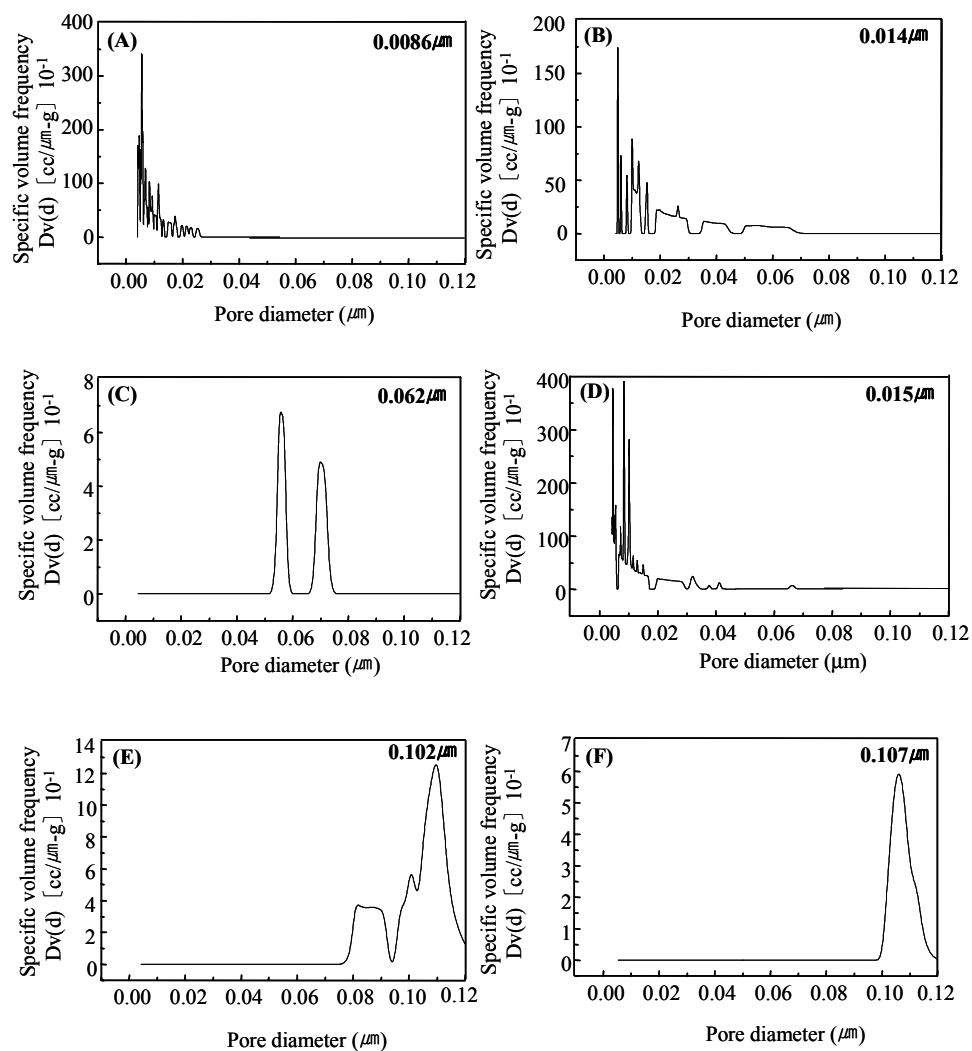


Fig. 4-3 Pore size and distributions of MLCCs after burnout process in ambient atmosphere: (A) 1°C/min to 200°C, (B) 1°C/min to 250°C, (C) 1°C/min to 300°C, (D) 3°C/min to 250°C, (E) 3°C/min to 300°C, and (F) 5°C/min to 300°C.

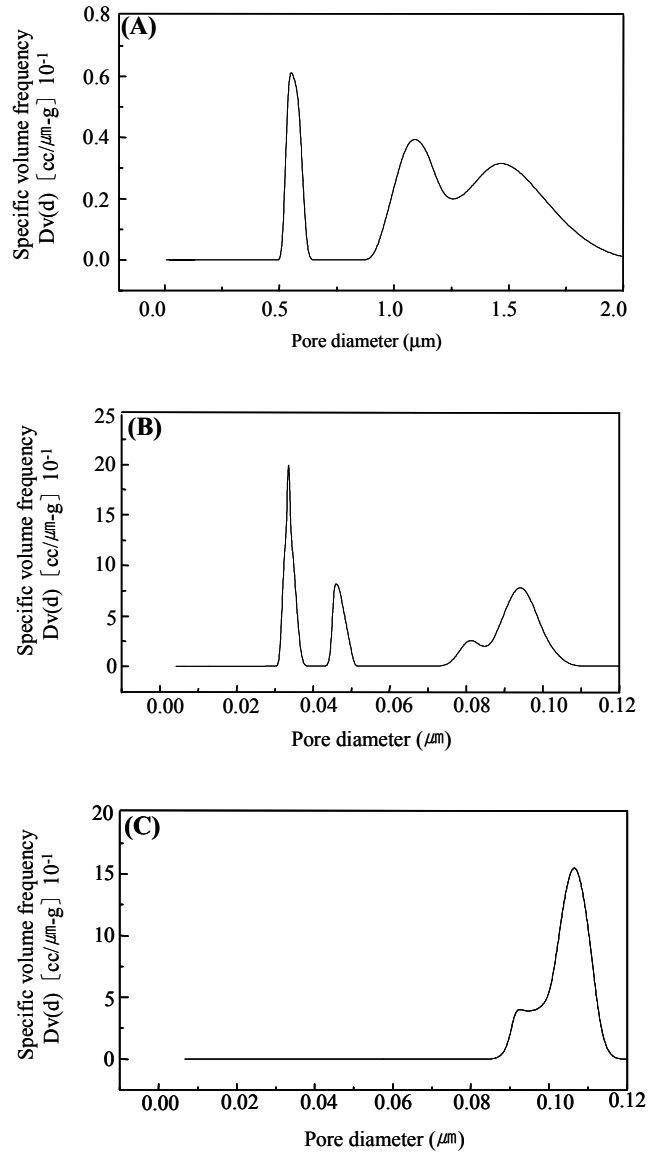


Fig. 4-4 Pore size and distributions of MLCCs after burnout process in reducing atmosphere: (A) $1^\circ\text{C}/\text{min}$ to 200°C , (B) $3^\circ\text{C}/\text{min}$ to 250°C , and (D) $5^\circ\text{C}/\text{min}$ to 300°C .

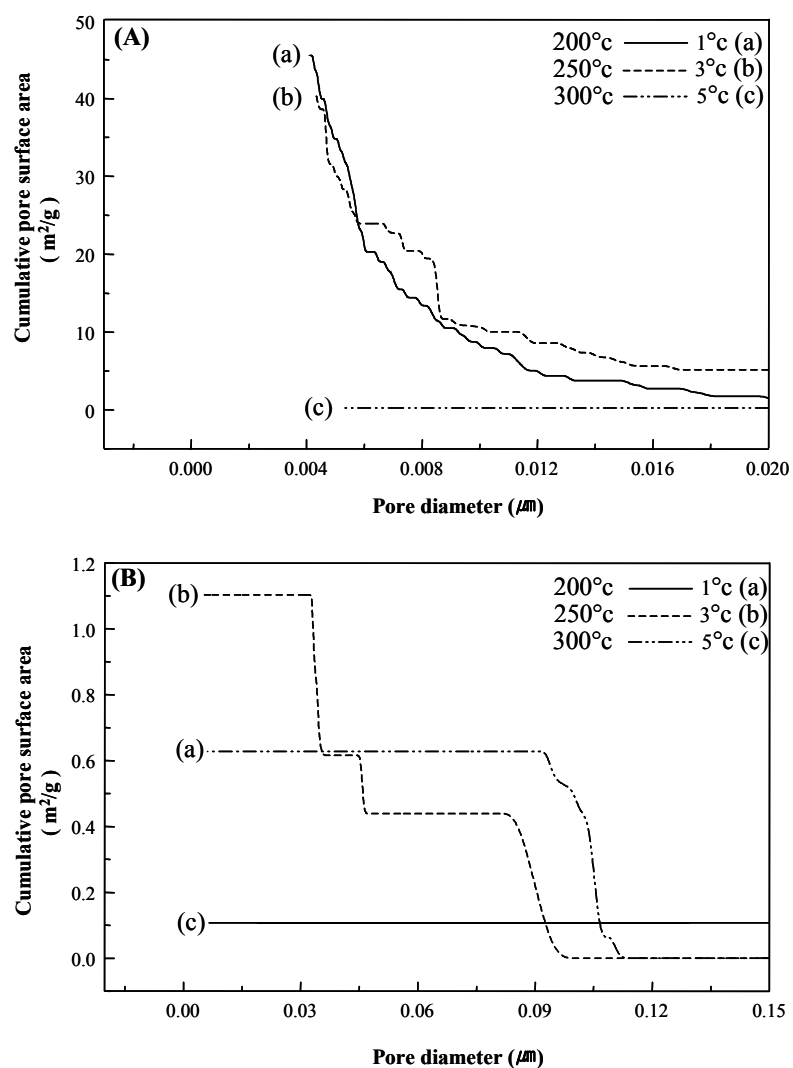


Fig. 4-5 Cumulative pore surface versus pore size of MLCCs after burnout process in both atmospheres: (A) ambient atmosphere with (a) 1°C /min to 200°C, (b) 3°C/min to 250°C, and (c) 5°C/min to 300°C; (B) reducing atmosphere with (a) 1°C/min to 200°C, (b) 3°C/min to 250°C, and (c) 5°C/min to 300°C.

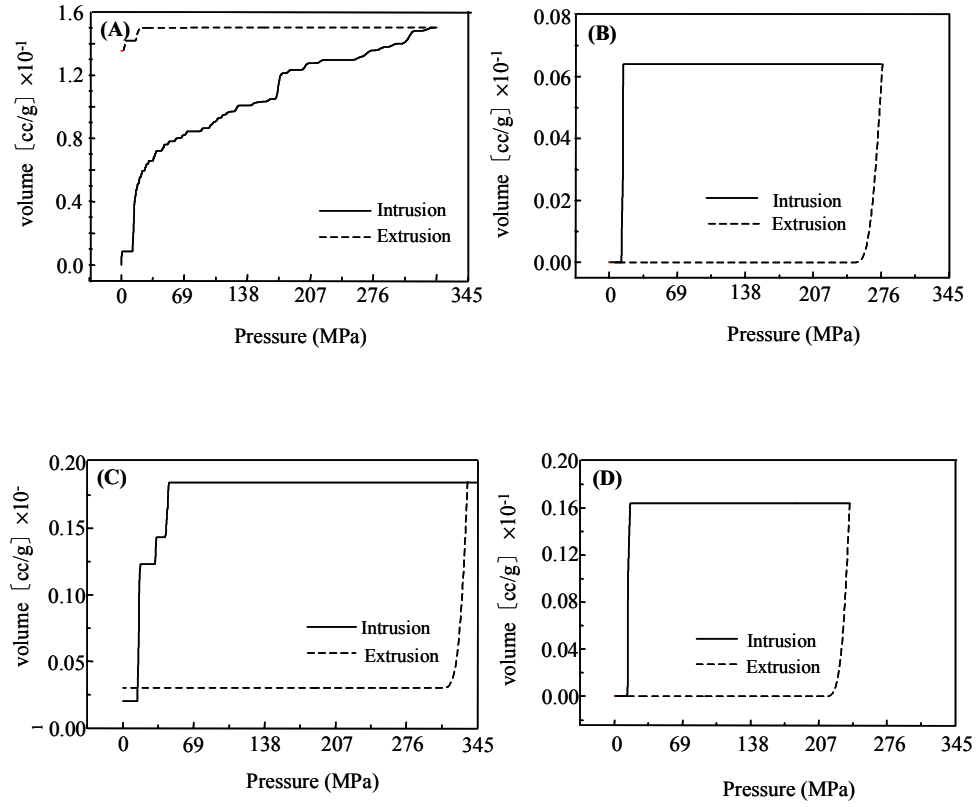


Fig. 4-6 Intrusion-extrusion curves of MLCCs after burnout process in both atmospheres: (A) 3°C/min to 250°C in ambient atmosphere, (B) 5°C/min to 300°C in ambient atmosphere, (C) 3°C/min to 250°C in reducing atmosphere, and (D) 5°C/min to 300°C in reducing atmosphere.

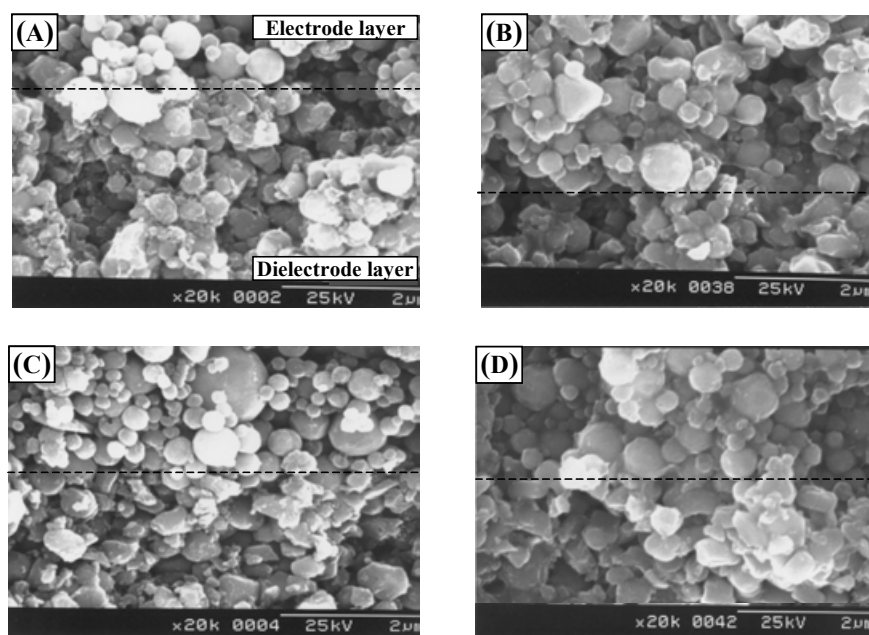


Fig. 4-7 SEM micrographs of MLCCs after burnout process in both atmospheres: (A) 1°C/min to 250°C in ambient atmosphere, (B) 1°C /min to 250°C in reducing atmosphere, (C) 5°C/min to 250°C in ambient atmosphere, (D) 5°C/min to 250°C in reducing atmosphere.

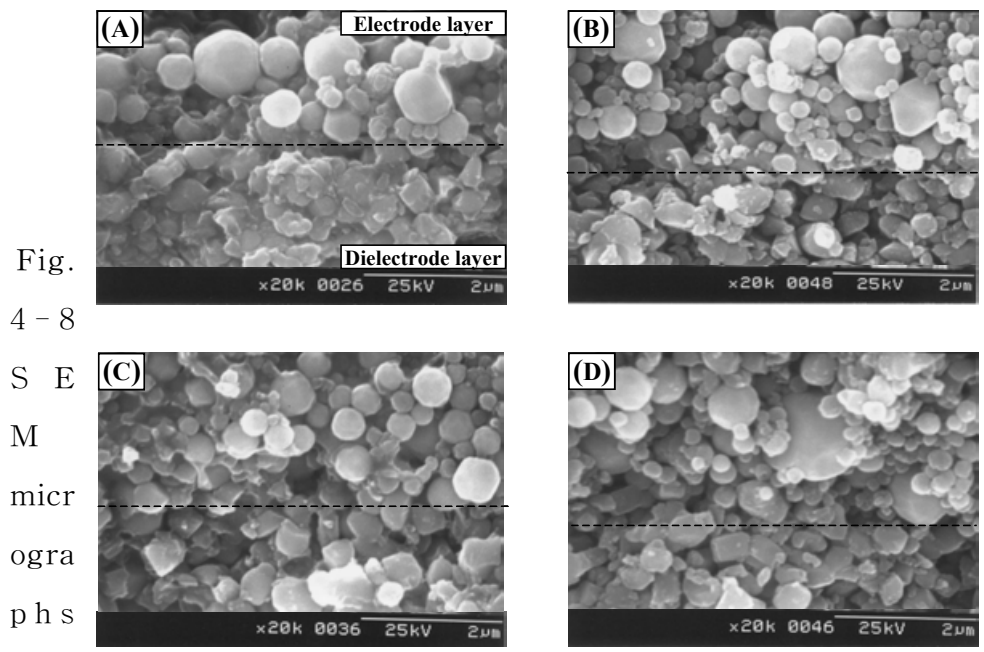


Fig. 4-8
SEM micrographs

of MLCCs after burnout process as functions of heating rate and temperature in reducing atmosphere: (A) 1°C/min to 200°C, (B) 1°C/min to 300°C, (C) 5°C/min to 200°C, and (D) 5°C /min to 300°C.

4.4 Conclusions

The burnout behavior of BaTiO₃ based Ni-MLCCs, showing Y5V characteristic, have been investigated by controlling atmosphere, temperature, and heating rate. The delamination in MLCCs is created at faster heating rate in the ambient atmosphere, independent of

temperature. However, MLCCs prepared under the reducing atmosphere ($\text{Ar}/\text{H}_2 = 97/3$) do not present any defects such as the delamination and cracks observed in the ambient atmosphere to the heating rate of 7°C . Pore size is increased with increases in temperature and heating rate, resulting in mono-modal distribution at higher temperature and faster heating rate. The pore size distribution is affected by heating rate in preference to temperature. On the other hand, MLCCs in the reducing atmosphere display smaller cumulative pore area surface than that of the ambient atmosphere. Even the ambient atmosphere is more effective to remove the binder rather than the reducing atmosphere, which will give some disadvantage to the post process because the binder can be removed suddenly. The effects of temperature and atmosphere on the burnout microstructure are superior to that of heating rate.

Chapter 5. Pore evolution and microstructure with heating profile in BaTiO_3 based Ni-MLCCs with Y5V specification

5.1. Introduction

Barium titanate (BaTiO_3) based multilayer ceramic capacitors (MLCCs) using base metal (nickel: Ni) as electrodes are widely used for electronic components^{9,23,25}. The technology in the fabrication of MLCCs has progressed enough to effectively reduce the thickness of the active layer, keeping in line with the miniaturization of electronic packages³⁻⁵. For which, precise control of the heating profile in the burnout and sintering processes has to be followed because the electrical properties and reliability of MLCCs are strongly dependent on its microstructure, which is determined by processing techniques^{44,45} and by grain growth inhibitors^{46,47}

A significant amount of residual pores are formed after binder burnout, showing porosity of 40 – 50 vol%, even though they disappear during the sequential sintering process. There have been numerous studies of advanced binder-solvent systems aiming to reduce the content of binders with better performance^{12,13}, including compaction techniques during multilayer ceramic fabrication¹⁴. Also, there are many citations where the relationships between the microstructure and electrical properties are described⁴⁴⁻⁴⁷. However, no citation was identified where pore evolution and microstructure were used to improve the reliability of MLCCs with a very thin active layer, although the cofiring behavior and/or sintering behavior of some dielectric materials have been reported^{26,48}. Specially the effects of the heating profile in the burnout and sintering processes on pore evolution and microstructure have not been

revealed, including what might be the major effect on pore evolution and microstructure of MLCCs. Therefore, the estimation and understanding of pore evolution and microstructure with respect to the heating profile in the burnout and sintering processes are essential for improving the electrical properties and reliability through the optimized fabrication process of MLCCs.

The present paper describes the influences of the heating profile, especially the heating rate and holding time, in both processes on pore evolution and microstructure in BaTiO₃ based Ni-MLCCs. The purpose of this study is to clarify how pores can be removed and what microstructure will be formed with the heating profile in both processes. The relationships among the heating rate in both processes, holding time, pore size and distribution, pore evolution, and microstructure are extensively discussed.

5.2. Experimental procedure

The dielectric material employed in this work was that with Y5V characteristics whose main composition is Ba_{0.95}Ca_{0.5}Ti_{0.82}Zr_{0.18} (Kyorix Co., Japan) + various metal oxide additives (such as Y₂O₃, MnO₂, SiO₂), totaling less than 4 wt% of the formulation. Ni powder was used as the internal electrode.

The green MLCCs were prepared using the following procedures. The powder mixtures and appropriate organic binders (PVB series) were dispersed in a nonaqueous media. The green sheet with a thickness of

9.5 m was prepared by the so-called slot-die method. After the Ni electrode was printed on the green sheet, it was laminated and isotropic pressed and cut into green chips. The final dimensions of the green MLCCs after cutting were 3.5×1.7×1.6 mm with 150 actives.

The burnout temperature to remove the organic binders was selected as 250°C, based on the previous study⁴⁹. The sintering process was performed in the reducing atmosphere ($P_{O_2} = 10^{-11} \sim 10^{-13}$) from 1000°C to 1200°C at intervals of 100°C without holding time except at 1200°C. In the case of 1200°C, sintering was done with and without a holding time of 3 hours, and the effects of the holding time on pore evolution and microstructure were investigated. The heating rate in both processes was controlled at rates of 1°C/min to 5°C/min with 2°C intervals two case studies were conducted. In the first case, the heating rate was changed in both processes and in the second case, the heating rate was change only in the sintering process with a fixed heating rate of 5°C/min in the burnout process.

Pore size distribution was measured using a mercury porosimetry (Autoscan-25, 60, Quantachrome Corp., Syosset, NY, USA), from which the cumulative pore surface area was compared with the heating rate and sintering temperature^{29,30,37}.

Also, hysteresis between the intrusion/extrusion behaviors was observed using a mercury porosimetry. The pore evolution and microstructure with respect to the heating rate, holding time, and sintering temperature, were observed in the fracture surface using a scanning electron microscope (SEM, S2700, Hitachi, Japan).

5.3 Results and discussion

The burnout and sintering behaviors of MLCCs are dependent on many variables, such as particle size, packing density, degree of agglomeration, sintering atmosphere and temperature, and the heating profile. Among these many variables, the effects of the heating profile, especially the heating rate and holding time, on pore evolution and microstructure were investigated. The schematic diagram of Fig. 5-1 shows the two cases previously described. The variable that had the strongest impact on the final microstructure of the MLCCs and the process in which it occurred were identified, and the way in which the pore evolution and microstructure affected was verified by the following results.

Mercury porosimetry is one of the methods to obtain information about the pore structure of a material^{29,30,37,50}. The pore size distribution and cumulative pore surface area can be measured from the value of an intrusion curve. Fig. 5-2 shows the pore size distribution after sintering in the reducing atmosphere ($P_{O_2}=10^{-11}\sim 10^{-13}$) at each heating rate and sintering temperature. Figs. 5-2(A-1), 5-2(B-1), and 5-2(C-1) show the pore size distribution at the heating rates of 1°C, 3°C, and 5°C /min at a temperature of 1100°C, respectively. The effect of the sintering temperature on the pore size distribution can be seen by comparing Figs. 5-2(B-1) and 5-2(B-2) or Figs. 5-2(C-1) and 5-2(C-2) for the same heating rate. Most notably, Fig. 5-2(A-2) shows the pore

size distribution when the heating rate was 1°C/min to 1100°C in the sintering process with the fixed heating rate (5°C/min) in the burnout process.

The pore size distribution became broad and narrow with increases of the heating rate and sintering temperature, respectively, indicating that the pore size distribution was not measured when the heating rate was 1°C/min to 1200°C in both processes. The slow heating rate can give a higher driving force than the fast heating rate, which will be effective in removing pores and accomplishing densification. However, an increase of the heating rate in the sintering process did not affect the pore size distribution, which was verified by comparing Figs. 5-2(A-2) and 5-2(C-1). The result indicates that the slow heating rate in the burnout process related to the rearrangement of particles played an important role in the pore size distribution. With a result of the pore size distribution, data on the hysteresis between the intrusion and extrusion behaviors could be obtained³⁴.

Fig. 5-3 shows the comparison between the intrusion and extrusion behaviors as functions of the heating rate and sintering temperature. The hysteresis in each case was very similar to each other except when the heating rate was 5°C/min in the burnout process (Figs. 5-3(A-2) and 5-3(C-1)). The volume of mercury that intruded increased and decreased with increases of the heating rate and sintering temperature, respectively. The first pressure for intrusion was delayed as the heating rate decreased, especially in the burnout process, and the sintering temperature increased. This result was very consistent with

the observation of the pore size distribution, as shown in Fig. 5-2. The effect of the heating rate in the burnout process on the hysteresis can be seen by comparing Figs. 5-3(A-1) and 5-3(A-2), showing no effect by the heating rate in the sintering process with similar hysteresis of Figs 5-3(A-2) and 5-3(C-1). Therefore, from the results of the pore size distribution and hysteresis, it is evident that the slow heating rate is more effective for pore evolution than the fast heating rate, and that control of the heating rate in the burnout process is more important than it is in the sintering process. However, it can be argued that pore shape and structure will be determined by the mercury intrusion/extrusion behaviors (hysteresis), because the amount of mercury retained by the sample will be influenced by a combination of at least two factors; the shape of the pores and the value of the contact angle³¹.

The effects of the heating rate and sintering temperature on pore evolution were more clearly observed in the cumulative pore surface area, as shown in Fig. 5-4. The cumulative pore surface area was reduced as the heating rate decreased in both processes (Fig. 5-4(A)) and the sintering temperature increased (Fig. 5-4(B)), showing a similar trend in the pore diameter contributed to the cumulative pore surface area. However, the effect of the heating rate on the cumulative pore surface area was less when the heating rate increased as 3°C/min and 5°C/min. Control of the heating rate in the burnout process was more effective in reducing the cumulative pore surface area than that in the sintering process, which was already verified in the previous results

(Figs. 5-2 and 5-3), even though the slow heating rate in the sintering process indicated a smaller cumulative pore surface area by comparing Figs. 5-4(A-c) and 5-4(B-a).

Fig. 5-5 shows the microstructure in the fracture surface with each heating rate at the sintering temperatures of 1100°C and 1200°C without holding time and again at 1200°C with a holding time of 3 hours. From that, the effect of the heating rate on the microstructure can be clarified. Two regions of the electrode and dielectric layers were distinguished with an increase of the sintering temperature. As evidence of the initial stage of densification, necking between particles was observed at the temperature of 1100°C (Figs. 5-5(A-1), 5-5(B-1), and 5-5(C-1)). The pore evolution rapidly progressed between 1100°C and 1200°C. The pore structure was closed at the heating rate of 1°C/min (Fig. 5-5(A-2) without holding time, showing the open pore channel at the heating rates of 3°C/min and 5°C/min (Figs. 5-5(B-2) and 5-5(C-2)). The pore structure, the closed pore structure in Fig. 5-5(A-2) and the open pore structure in Figs. 5-5(B-2) and 5-5(C-2), could be verified with the results of the pore size distribution in Fig. 5-2. Even though the holding time was given in the sintering process, the final microstructure was also affected by the heating rate in the burnout process and by the previous microstructure, showing the residual pores at heating rates above 1°C/min.

The results indicate that the slow heating rate was more effective in reducing pores than the fast heating rate. Full densification was achieved with the holding time of 3 hours at the heating rate of 1°C

/min (Fig. 5-5(A-3)), showing the residual pores at the heating rates of 3°C/min and 5°C/min (Figs. 5-5(B-3) and 5-5(C-3)). There was a critical heating rate for the full densification of the MLCCs, indicating that control of the heating rate was more important than control of the holding time in determining the final microstructure.

However, it cannot be determined from the results of Fig. 5-5 which heating rate and in which process will mainly affect pore evolution and microstructure. Fig. 5-6 shows the microstructures at the heating rates of 1°C/min (A series) and 3°C/min (B series) in the sintering process with the fixed heating rate in the burnout process (temperature of 250°C and heating rate of 5°C/min), and at the heating rates of 1°C/min and 5°C/min in the burnout and sintering processes, respectively (C series). The microstructures without the holding time of Figs. 5-6(A-1) and 5-6(B-1) and with the holding time of Figs. 5-6(A-2) and 5-6(B-2) were similar to the microstructures of Figs. 5-5(C-2) and 5-5(C-3), respectively, even though the heating rates in the sintering process were different. Therefore, the heating rate in the sintering process did not have any effect on the microstructure when the heating rate in the burnout process was fast and same (5°C/min in this study). Meanwhile, when the heating rate in the burnout process was 1°C/min, the pores were almost completely removed as shown in Fig. 5-6(C-2), showing an intermediate microstructure between Fig. 5-5(A-3) and 5-5(C-3). This indicates that the heating rate in the sintering process partially affected the pore evolution and microstructure. Also, the pore evolution progressed with the holding time. However, the final microstructure

showed the residual pores when the heating rate in the sintering process was fast (Fig. 5-6(C-2)), independent of the heating rate in the burnout process. Therefore, it can be postulated that if the heating rate is selected as 3°C/min in the sintering process at the heating rate of 1°C/min in the burnout process, the MLCCs will be fully densified.

As a result, the burnout process related to the rearrangement of particles and the removal of organic binders was more important than the sintering process in the fabrication process of the MLCCs, and control of the heating rate in the burnout process was more effective for pore evolution than that in the sintering process, even though the heating rate in the sintering process partially affected the final microstructure. The holding time was also effective in removing the residual pores and in developing the final microstructure. In this system, pore evolution rapidly progressed between 1100°C and 1200°C, showing the effect of the heating rate in the burnout process, and full densification was achieved at the heating rate of 1°C/min in both processes.

- Case I : Change heating rate in both processes (1, 3, 5°C/min)
- CaseII: Change heating rate only in sintering process
(5°C/min heating rate fixed in burnout process)

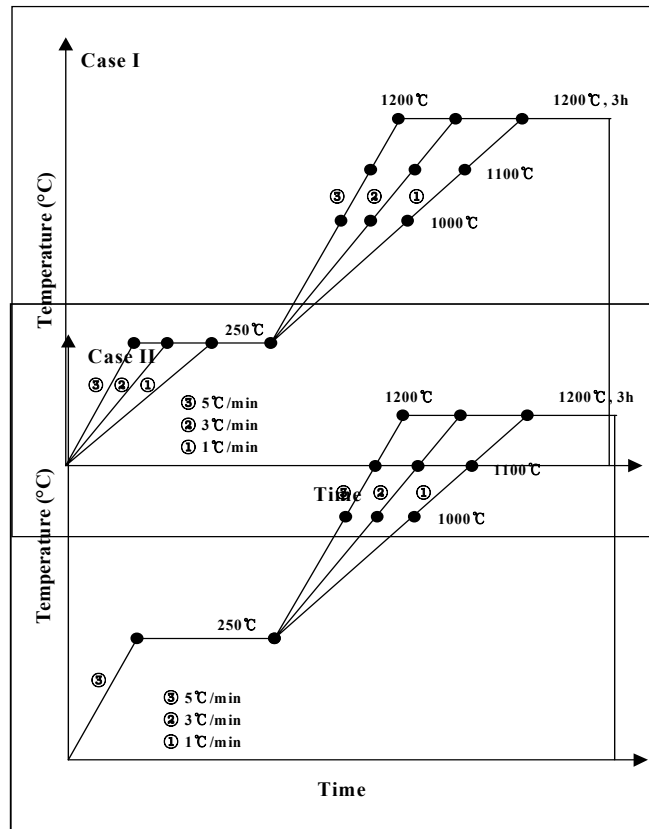
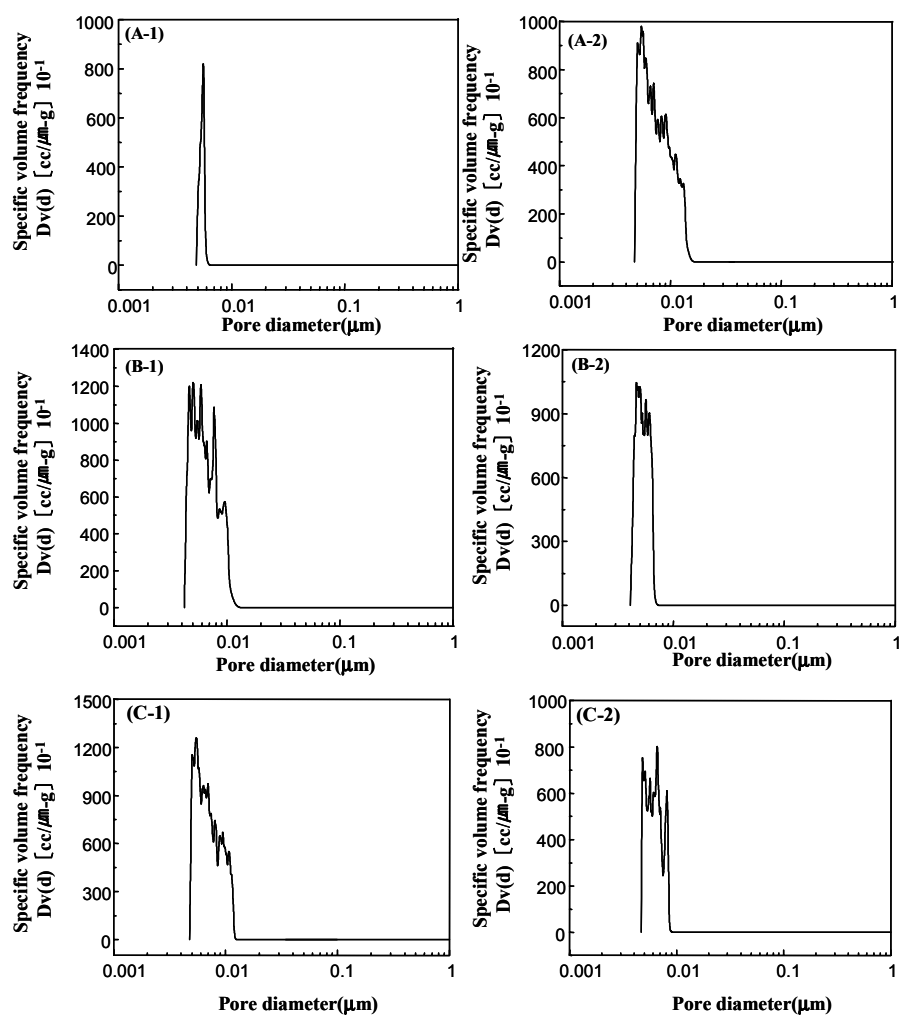


Fig. 5-1 Schematic diagram of heating profile in both processes, with changing heating rate in both processes and only in sintering process

Fig. 5-2 Pore size distributions at various heating rates and sintering temperatures: (A-1) 1 °C/min to 1100 °C in both processes, (A-2) 1 °C/min in the burnout process and 5 °C to 1100 °C in the sintering process, (B-1) 3 °C/min to 1100 °C in both processes, (B-2) 3 °C/min to 1200 °C in both processes, (C-1) 5 °C/min to 1100 °C in both processes, and (C-2) 5 °C/min to 1200 °C in both



processes.

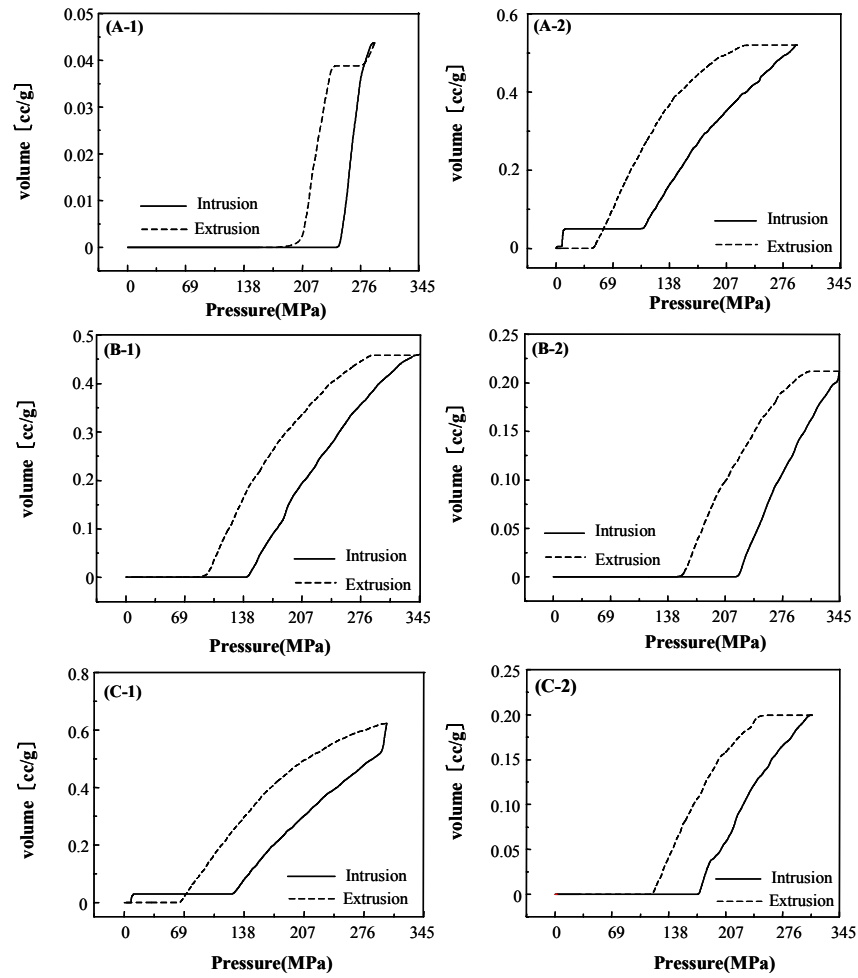


Fig.
5 - 3
Intru
sion
and
extr

usion behaviors of the MLCCs at various heating rates and sintering temperatures: (A-1) 1°C/min to 1100°C in both processes, (A-2) 1°C/min in the burnout process and 5°C to 1100°C in the sintering process, (B-1) 3°C/min to 1100°C in both processes, (B-2) 3°C/min to 1200°C in both processes, (C-1) 5°C/min to 1100°C in both processes, and (C-2) 5°C/min to 1200°C in both processes.

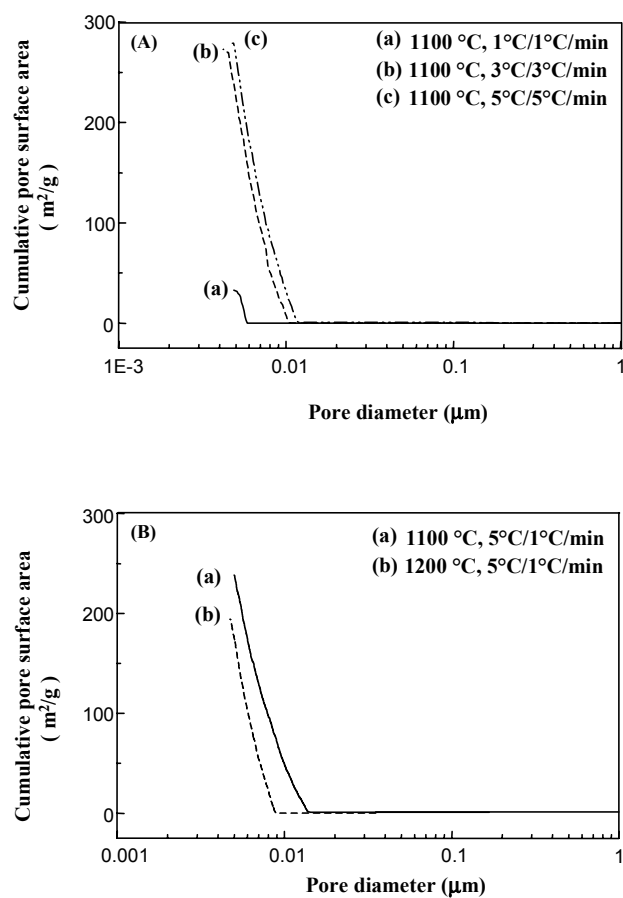


Fig. 5-4 Cumulative pore surface area as functions of heating rate and sintering temperature: (A) heating rates in both processes of (a) 1 °C/min, (b) 3 °C/min, and (c) 5 °C/min to 1100 °C and (B) sintering temperatures of (a) 1100 °C and (b) 1200 °C with fixed heating rates of 5 °C/min and 1 °C/min in burnout and sintering processes, respectively.

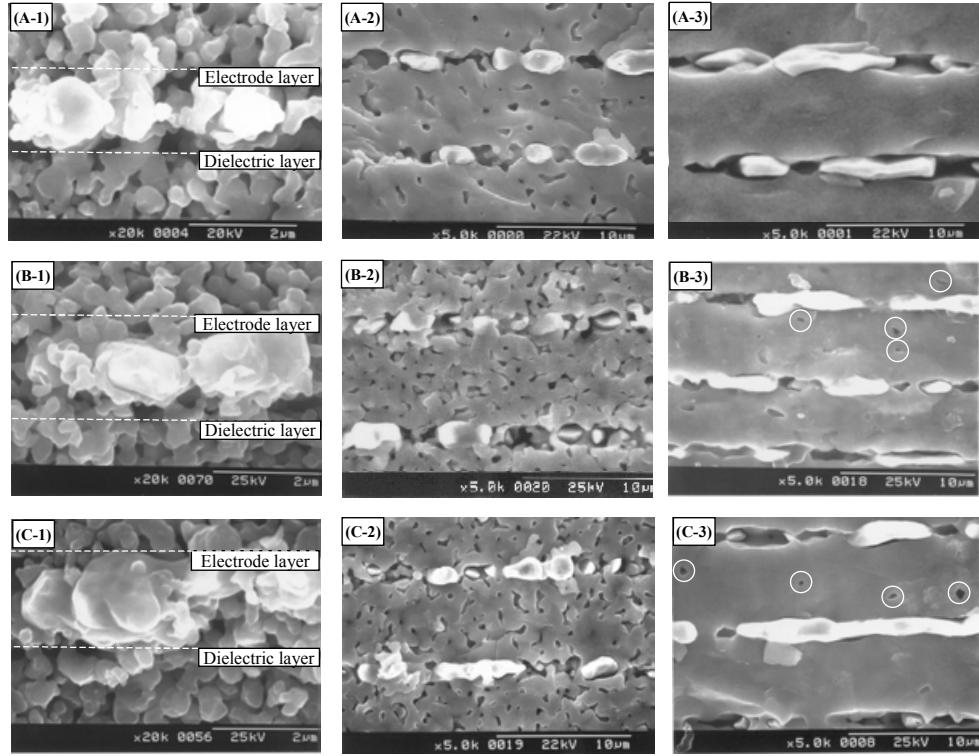


Fig. 5-5 Fracture micrographs of the MLCCs at different heating rates and sintering temperatures: (A-1), (B-1), and (C-1) 1100°C without holding time, (A-2), (B-2), and (C-2) 1200°C without holding time, and (A-3), (B-3), and (C-3) 1200°C with holding time of 3 hours. (A), (B), and (C) series indicate different heating rates of 1°C/min, 3°C/min, and 5°C/min in both processes, respectively. The mark of an open circle represents a pore in the dielectric layer.

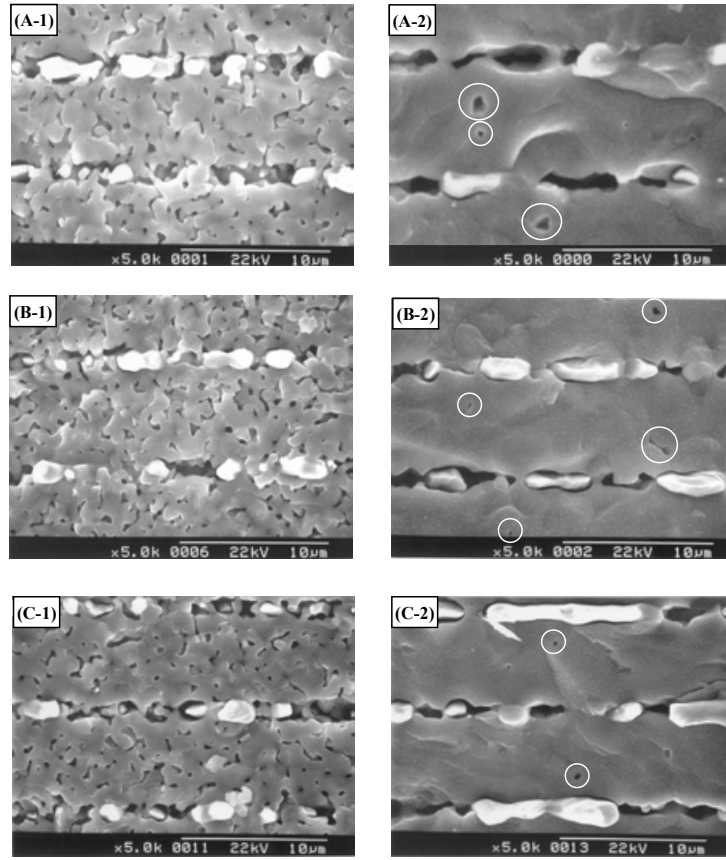


Fig. 5-6 Fracture surface of the MLCCs at different heating rates in both processes with and without holding time at 1200°C: (A-1), (B-1), and (C-1) without holding time, and (A-2) (B-2), and (C-2) with holding time of 3hours. (A) and (B) series indicate the different heating rates of 1°C/min and 3°C/min in the sintering process with a fixed heating rate of 5°C/min in the burnout process. (C) series were heat-treated at the heating rates of 1°C/min and 5°C/min in the burnout and sintering processes, respectively. The mark of an open circle represents a pore in the dielectric layer.

5.4 Conclusions

The pore size distribution became narrow with a decrease and an increase of the heating rate and sintering temperature, respectively, showing no effect by the heating rate in the sintering process. The results of the hysteresis and cumulative pore surface area are very consistent with the results of the pore size distribution, indicating that the effect of the heating rate in the burnout process was superior to that in the sintering process. The necking between particles was observed at the temperature of 1100°C and pore evolution rapidly progressed between 1100°C and 1200°C. Control of the heating rate in the burnout process was more important than that in the sintering process for pore evolution, even though the heating rate in the sintering process partially affected the final microstructure, indicating that the rearrangement of particles finished during the binder burnout process continued to affect the sintering process. The holding time was also effective in removing the residual pores and in developing the final microstructure. Consequently, the slow heating rate was more effective in removing pores and there was a critical heating rate in the sintering process to achieve full densification, independent of the heating rate in the burnout process. The heating rate for full densification was 1°C/min in both processes with the holding time in this system.

Chapter 6. Pore evolution and microstructural development in Ni-MLCCs with X7R characteristic

6.1. Introduction

In ceramic capacitors, barium titanate (BaTiO_3) is used extensively as the dielectric layer, particularly due to its high dielectric constant and low loss characteristics⁴⁹. One of various capacitors, multilayer ceramic capacitors (MLCCs) with Ni base metal electrodes (BME) have been increasingly produced to meet growing requirements for miniaturization, high capacitance, and cost reduction^{23,6}. Especially, MLCCs specified with X7R characteristic are greatly appreciated because of their high volumetric efficiency and the temperature-compensated capacitance response, which shows chemically heterogeneous microstructure in a grain, so called core-shell structure^{3,9}. However, a major problem of BME is that MLCCs have to be fired in a reducing atmosphere to prevent the Ni oxidation, showing that normal BaTiO_3 based dielectrics decrease the insulation resistance (IR) with 10–12 orders of magnitude after sintering in forming gas (H_2/N_2)^{6-11,24}.

Previously, we have reported that the atmosphere and temperature in

the burnout process play a more important role in preventing the defects and in controlling the burnout microstructure in MLCCs specified with X7R characteristic than the heating rate⁵⁰. However, this does not mean the high density and desired electrical properties of the final products after sintering due to the possible presence of drying or burnout defects, for example, delamination or cracking of the sheets. Also, the study on the pore evolution and sintering microstructure in MLCCs with Y5V specifications indicated that control of the heating rate in the burnout process is a more effective in removing the residual pores than that in the sintering process, showing the effect of the sintering temperature on developing the final microstructure⁵¹.

Therefore, the burnout process associated with rearrangement of particles and removal of organic binders in the fabrication process of MLCCs needs to control the pore evolution and to achieve full densification. There are many reports about the burnout process for preventing the oxidation of BME and controlling the residual carbon from organic binders^{3,22,24,50} as well as reports about relationships between microstructure and electrical properties^{3,6-9,51}. Even though the cofiring characteristics and dielectric properties for dielectric composites with X7R characteristics have been reported^{6,9,10,46}, the effects of heating rate on pore evolution and sintering microstructure of BaTiO₃ based Ni-MLCCs specified X7R characteristic, have not been shown in the

literature. Therefore, the understanding and investigation of the roles of the heating profiles in the burnout and sintering processes related to the pore evolution and microstructural development are essential for improving the dielectric properties and reliability of MLCCs with BME.

The present work describes the influences of heating profiles, especially heating rate, sintering temperature, and holding time in both burnout and sintering processes, on the pore evolution and microstructural development in BaTiO₃ based Ni-MLCCs with X7R specification. The objective of this present study is to clarify when and how pores can be removed and microstructure formed with the heating profiles in both processes. The results presented by pore evolution and microstructural development with heating rate, sintering temperature, and holding time were extensively discussed as well.

6.2. Experimental procedure

6.2.1. Materials and Preparation

BaTiO₃ (BT-04B, Sakai Co., Japan) and Ni powders with glass frit were used as the dielectric material and internal electrode. The dielectric formulation showing X7R characteristic was prepared by doping various metal oxide additives (Y₂O₃, MgCO₃, MnO₂, V₂O₅, Cr₂O₃) and glass frit (Ba-Ca-Si system), totaling less than 4wt% of the formulation. Ni powder was used as internal electrode.

The green MLCCs were prepared by the following procedure. The powder mixtures and appropriate organic binder (PVB series) were dispersed in a nonaqueous media (mixture of toluene and ethanol). The green sheet with the thickness of 4 μ m was prepared by a so-called slot-die method. After Ni electrode was printed on the green sheet, which was laminated and isotropically pressed and cut to green chips. The final dimensions of the green MLCCs after cutting were 4 \times 2 \times 2 mm with 330 actives.

6.2.2. Heat treatment

The burnout temperature to remove organic binders could be selected as 250 $^{\circ}$ C based on the previous study⁵⁰. The sintering process was performed in the reducing atmosphere (P_{O_2} =10⁻¹¹~10⁻¹³) from 1100 $^{\circ}$ C to 1300 $^{\circ}$ C with intervals of 100 $^{\circ}$ C without the holding time except at 1300 $^{\circ}$ C. In the case of 1300 $^{\circ}$ C, sintering was done with and without the holding time of 3h, and the effects of the holding time on the pore evolution and microstructural development were investigated. The heating rate in both processes was controlled as 1 $^{\circ}$ C/min, 3 $^{\circ}$ C/min, and 5 $^{\circ}$ C/min. In addition, other two case studies were done in order to observe which is a main factor in removing the residual pores: the first case, the heating rates in the burnout and sintering processes were fixed as 5 $^{\circ}$ C/min and 1 $^{\circ}$ C/min, respectively, and the second case, the heating rates were reversed. The effects of holding time and temperature on the microstructural development were investigated,

controlling the temperature of 1200°C and 1250°C and the holding time of 3h and 6h.

6.2.3. Characterization

Pore size and distribution for the heat treated MLCCs was measured by a mercury porosimetry (Autoscan-25, 60, Quantachrome Corp., Syosset, NY, USA), from which cumulative pore surface area and hysteresis between the mercury intrusion/extrusion behavior were compared with the heating rate and sintering temperature^{28,35}. The microstructural development with the heating rate, sintering temperature, and holding time were observed in the fracture surface by a scanning electron microscope (SEM, S2700, Hitachi, Japan).

6.3 Results and discussion

6.3.1. Pore evolution

The main variables affecting sinterability and microstructure of green body can be divided by tow variables related to raw materials (powder shape, size, size distribution, and impurity) and to sintering condition (temperature, time, pressure, atmosphere, heating rate, and holding time)⁵². The pore evolution and microstructural development with the sintering condition associated with thermodynamical variable, especially

heating rate, were focused on this study. The roles of holding time and temperature under condition of same heating rate were compared.

Mercury porosimetry is based on the fact that mercury is non-wetting liquid. Thus, mercury penetration into pore spaces occurs exclusively when pressure is applied. Then pore size and distribution can be obtained according to the radii calculated using the Washburn equation⁵³, where pore radius is inversely proportional to the applied pressure^{30,41}. Fig. 6-1 shows the pore size distribution of MLCCs after sintering in the reducing atmosphere ($P_{O_2}=10^{-11}\sim 10^{-13}$) with the heating rate and temperature. To identify the effect of heating rate in the same temperature, Figs. 6-1(A-1), 2(B-1), and 6-1(C-1) show the pore size distribution at the heating rate of 1°C, 3°C, and 5°C/min at the temperature of 1200°C, respectively. The different pore size distribution according to the temperature of 1200°C and 1300°C was observed in the heating rate of 3°C/min and 5°C/min. Most notably, Fig. 6-1(A-2) shows the pore size distribution in the case of the heating rate of 1°C/min to 1200°C in the sintering process with the fixed heating rate of 5°C/min in the burnout process.

The pore size distribution became narrow with an increase of the sintering temperature and broad with an increase of the heating rate, indicating that the pore was not detected in the case of the heating rate of 1°C/min in both processes at 1300°C. The pore size distribution at the heating rate of 5°C/min and 1°C/min in the burnout and sintering processes (Fig. 6-1(A-2)), respectively, was a broader than that with the heating rate of 1°C/min in the both processes (Fig. 6-1(A-1)), which

was similar to that with the heating rate of with 5°C/min in the both processes (Fig. 6-1(C-1)). It was verified that the slow heating rate in the burnout process is a more effective in removing pores and accomplishing densification than the high heating rate, indicating that an increase of the heating rate in the sintering process did not affect the pore size distribution.

Fig. 6-2 shows hysteresis between the intrusion and extrusion behaviors as functions of the heating rate and sintering temperature. The volume of mercury that intruded increased and decreased with increases of the heating rate and sintering temperature, respectively. The first pressure for intrusion was delayed as the heating rate decreased, especially in the burnout process, and the sintering temperature increased. The hysteresis of Fig. 6-2(A-2) is similar to that of Fig. 6-2(C-1), indicating that the heating rate in the burnout process is a more effective in removing the residual pore and in developing the microstructure than that in the sintering process. The volume of mercury in the low sintering temperature (Fig. 6-2(A-1)) was smaller than those in the high one (Fig. 6-2(B-2) and 6-2(C-2)), which indicates that the slow heating rate in the burnout process related to rearrangement of particles and removing of organic binders were a more effective in improving the pore evolution than high temperature associated with sintering driving force in the sintering process.

From information about intrusion/extrusion behaviors, the pore structure and shape can predict, but results with mercury hysteresis used in this study is different with those of de Boers five types

measured by gas³². Therefore, it can be argued that mercury and gas intruded in samples will be influenced by the different property of liquid (mercury) and gas, because liquid (mercury) and gas is different with velocity and depth intruded in samples, and this will be affected by the value of angle contacted intruded in samples

The effects of heating rate and sintering temperature on the pore evolution were also observed with the information about the cumulative pore surface area. Fig. 6-3 shows the cumulative pore surface area with heating rate in the temperature of 1200°C (Fig. 6-3(A)) and with temperature in the same heating rate (Fig. 6-3(B)). The cumulative pore surface area was reduced as the heating rate decreased and the sintering temperature increased, even though the pore diameter contributed to the cumulative pore surface area was similar to each other.

Therefore, if the burnout process is performed with the fast heating rate, the binder can be removed suddenly which creates polymeric skinning and trapping of gas bubbles. This is also undesirable for the reason that particle movement is difficult along the diffusion path. On the other hand, the slow heating rate in the burnout process allows particles to move through the residual organic binders and promote the rearrangement in a longer period of the burnout process, forming the funicular or pendular particle surfaces. This rearrangement supported by the residual organic binders has a positive impact on particle packing and burnout microstructure, which may facilitate densification with a desired microstructure⁵⁴⁻⁵⁵.

6.3.2. Microstructural development

Fig. 6-4 shows microstructure in the fracture surface with each heating rate at the sintering temperatures of 1200°C and 1300°C without the holding time and 1300°C with the holding time of 3h. The effect of the heating rate verified from results of the pore size distributions and cumulative pore surface area can be clarified. Two regions of the electrode and dielectric layers were distinguished with an increase of the sintering temperature. As evidence of the initial stage of densification, necking between particles was observed at the temperature of 1200°C (Fig. 6-4(A-1), 6-4(B-1), and 6-4(C-1)). The pore evolution rapidly progressed between 1200°C and 1300°C.

The pore structure was closed at the heating rate of 1°C/min (Fig. 6-4(A-2)) without holding time, showing the open pore channel at the heating rates of 3°C/min and 5°C/min (Figs. 6-4(B-2) and 6-4(C-2)). The pore structure, the closed pore structure in Fig. 6-4(A-2) and the open pore structure in Figs. 6-4(B-2) and 6-4(C-2), could be verified with the results of the pore size distribution in Fig. 6-1. Even though the holding time was given in the sintering process, the final microstructure was also affected by the heating rate in the burnout process and by the previous microstructure, showing the residual pores at the heating rates above 1°C/min. This indicates again that the slow heating rate is a more effective in reducing the residual pores than the fast heating rate, which is operated to increase the sintering driving force in sintering mechanisms (grain boundary and volume diffusions)

affecting the final microstructure. The full densification was achieved at the heating rate of 1°C/min (Fig. 6-4(A-3)) with the holding time of 3h in, showing the residual pores in the heating rate of 3°C/min and 5°C/min (Fig. 6-4(B-3) and 6-4(C-3)). There was a critical heating rate for the full densification of MLCCs, indicating that the control of the heating rate was more important than that of the holding time in determining the final microstructure and the initial stage in the sintering process played an important role in the final microstructure.

Fig. 6-5 shows microstructure at the heating rate of 5°C/min and 1°C/min in the burnout and sintering processes, and at the heating rate of 1°C/min and 5°C/min in the burnout and sintering processes (Fig. 6-5(A and B series)), respectively. The effect of heating rate on the microstructural development (which heating rate will mainly affect the microstructural development) was identified as comparison of A and B series. Even though the heating rate was different in the sintering process, the microstructure of Fig. 6-5(B-1) was observed similar to the microstructure of Fig. 6-4(A-2), showing full densification with the holding time (Fig. 6-5(B-2)). When the heating rate in the sintering process was decreased as 1°C/min, the microstructures of A series was similar to those of Fig. 6-4(C-2) and 6-4(C-3). This means that the slow heating rate in the sintering process does not give any effect to the microstructure. It can be postulated that if the heating rate in the sintering process is decreased as 1°C/min with the heating rate of 3°C/min in the burnout process, MLCCs will be fully densified.

The effects of holding time and temperature associated with

sintering driving force in the sintering variables are important in achieving densification for sintering. Fig. 6-6 shows microstructure as functions of temperature and holding time in sintering process. The densification in the microstructure of Fig. 6-6(A-1) was progressed with the holding time of 3h compared to that of Fig. 6-4(C-1). However, when the holding time was increased from 3h to 6h, the effect of holding time was not investigated. When the sintering temperature increased to 1250°C, the pores were rapidly removed. Reminding the pore evolution rapidly progressed between 1200°C and 1300°C in Fig. 6-4, the temperature was now clarified. The microstructure of Fig. 6-6(B series) with the holding time at 1250°C was similar to that of Fig. 6-4(C-2) without holding time at 1300°C. This indicates that the holding time can compensate the low driving force by the low sintering temperature.

Based on the above results, it can be proposed that the heating rate in the burnout process is more important than that in the sintering process. The holding time have to be given to achieve the full densification in the final sintering temperature, but the sintering temperature is more effective in removing the residual pores and developing the microstructure than the holding time.

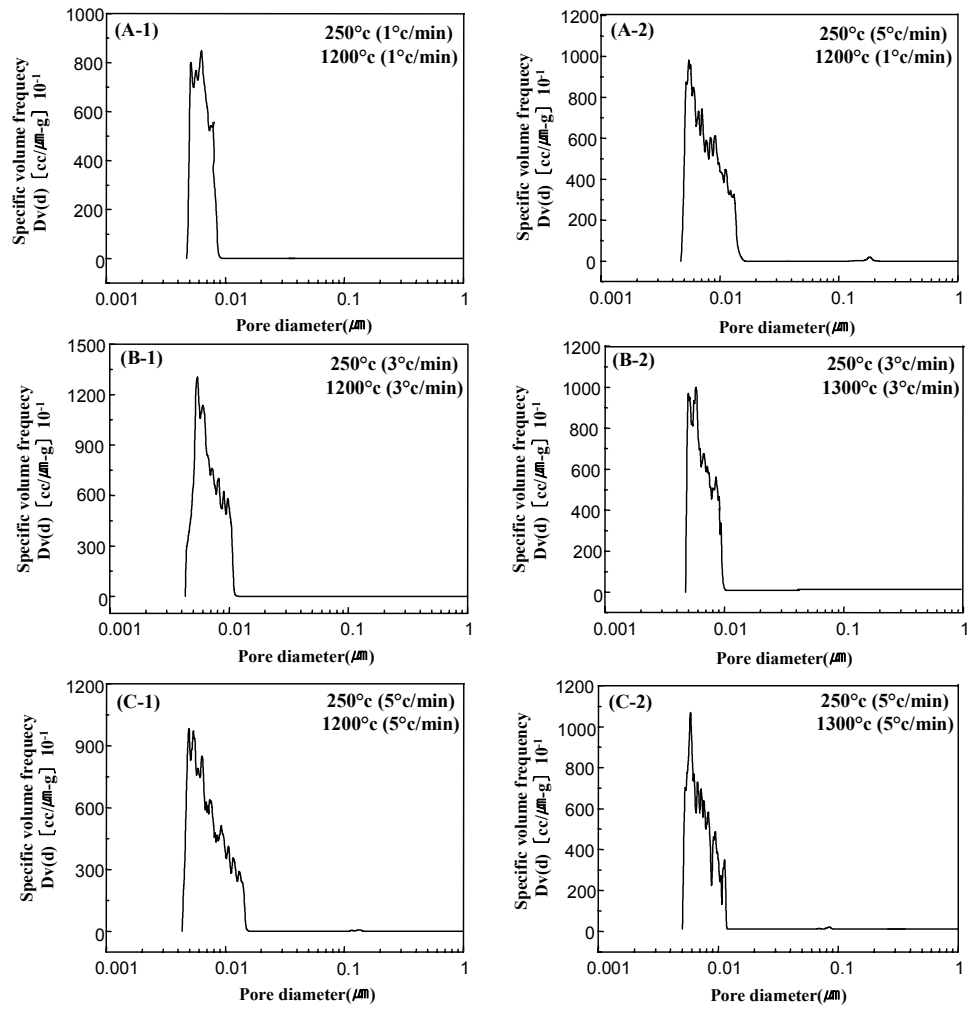


Fig. 6-1 Pore size and distributions with heating rate and sintering temperature: (A-1) 1°C/min to 1200°C in both processes, (A-2) 1°C/min in burnout process and 5°C to 1300°C in sintering process, (B-1) 3°C/min to 1200°C in both processes, (B-2) 3°C/min to 1300°C in both processes, (C-1) 5°C/min to 1200 °C in both processes, and (C-2) 5°C/min to 1300°C in both processes.

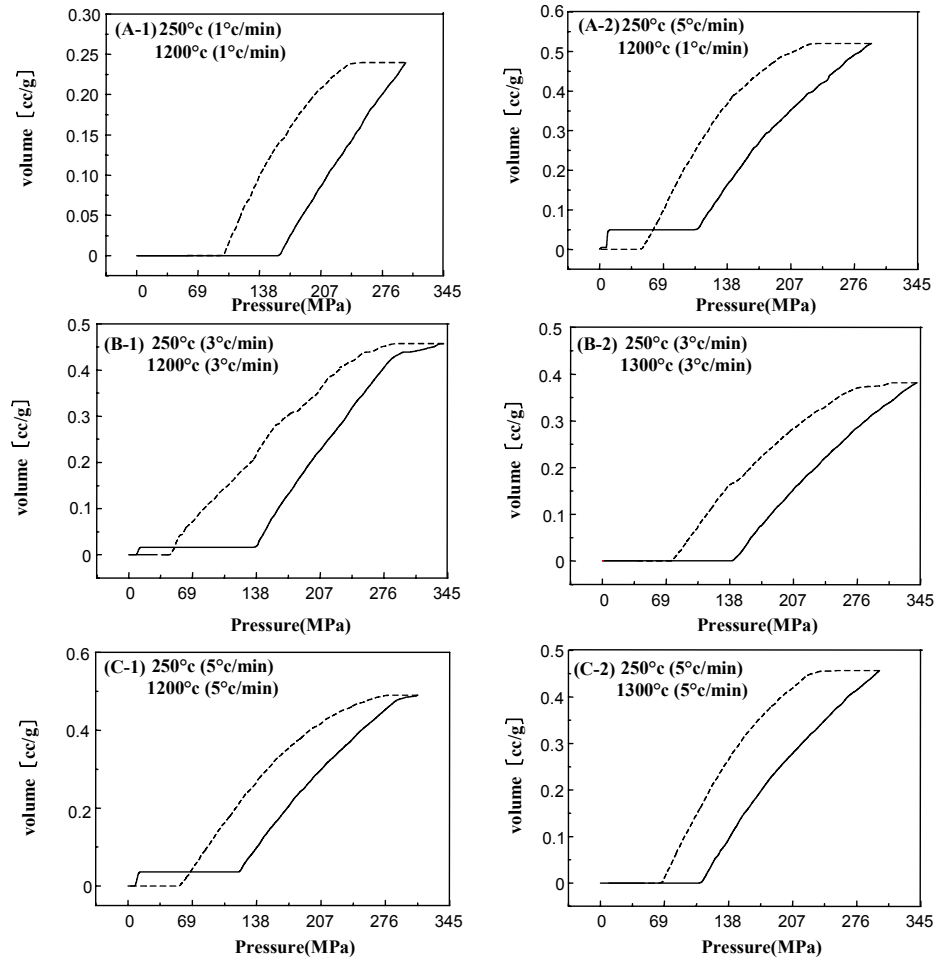


Fig. 6-2 Intrusion and extrusion behaviors of MLCCs with heating rate and sintering temperature: (A-1) 1°C/min to 1200°C in both processes, (A-2) 1°C/min in burnout process and 5°C to 1300°C in sintering process, (B-1) 3°C/min to 1200°C in both processes, (B-2) 3°C/min to 1300°C in both processes, (C-1) 5°C/min to 1200°C in both processes, and (C-2) 5°C/min to 1300°C in both processes.

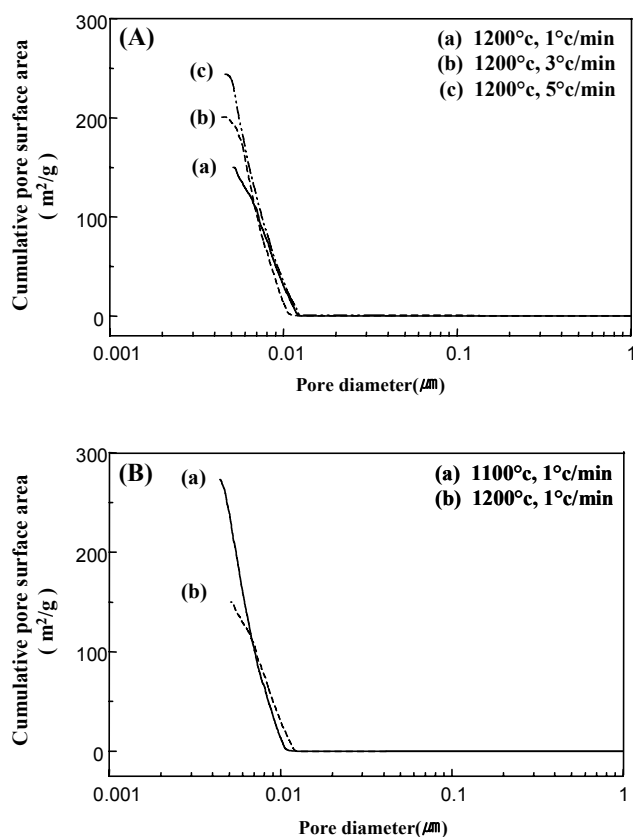


Fig. 6-3 Cumulative pore surface area as functions of heating rate and sintering temperature: (A) changing heating rate in both processes as (a) 1°C/min, (b) 3°C/min, and (c) 5°C/min to 1200°C and (B) changing sintering temperature as (a) 1100°C and (b) 1200°C with fixed heating rates of 1°C/min in both processes.

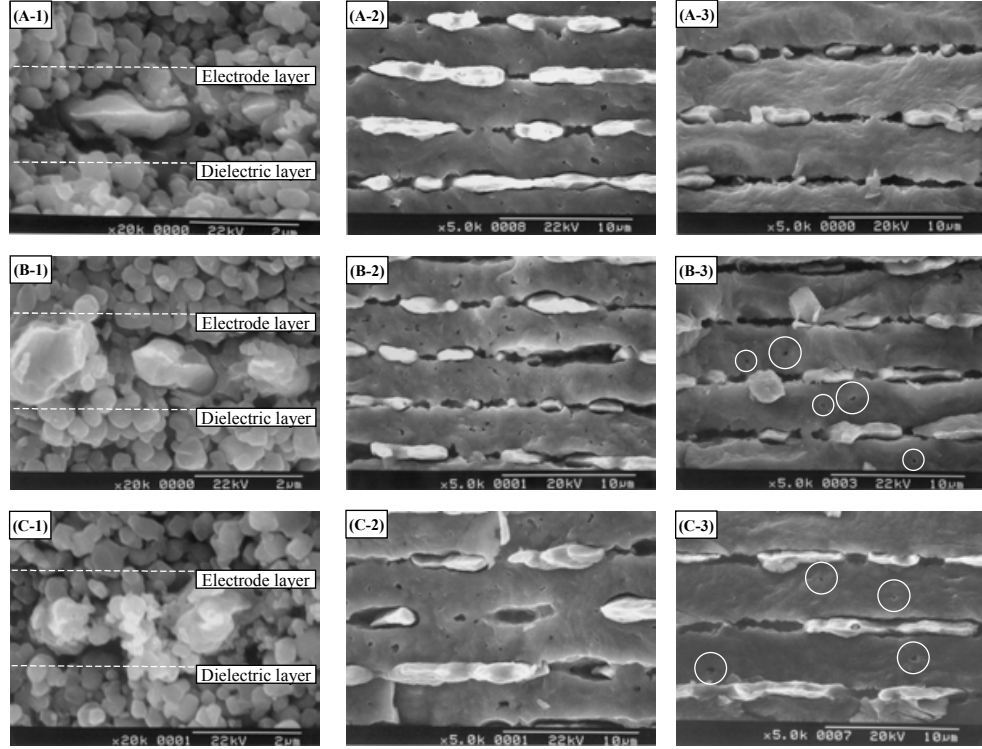


Fig. 6-4 Fracture micrographs of MLCCs with different heating rates of (A) 1°C/min, (B) 3°C/min, and (C) 5°C/min at each sintering temperature. Numerical series of (1), (2), and (3) in Figs (A), (B) and (C) indicate the sintering temperature of 1200°C without holding time, 1300°C without holding time, and 1300°C with holding time of 3h, respectively.

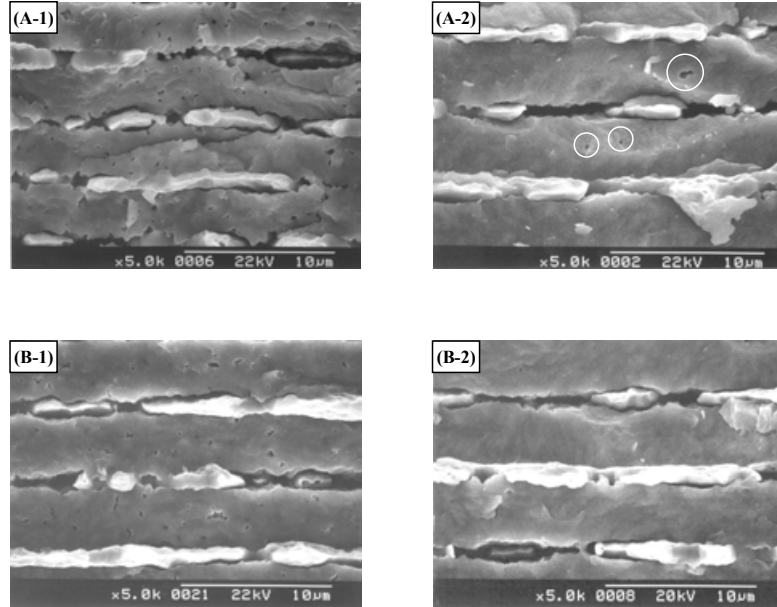


Fig. 6-5 Fracture micrographs of MLCCs with different heating rates in both processes with and without holding time at 1300°C: (A-1) and (B-1) without holding time, and (A-2) and (B-2) with holding time of 3h. (A) series indicate the heating rates of 5°C/min and 1°C/min in the burnout and sintering processes and (B) series reversed the heating rate in both processes.

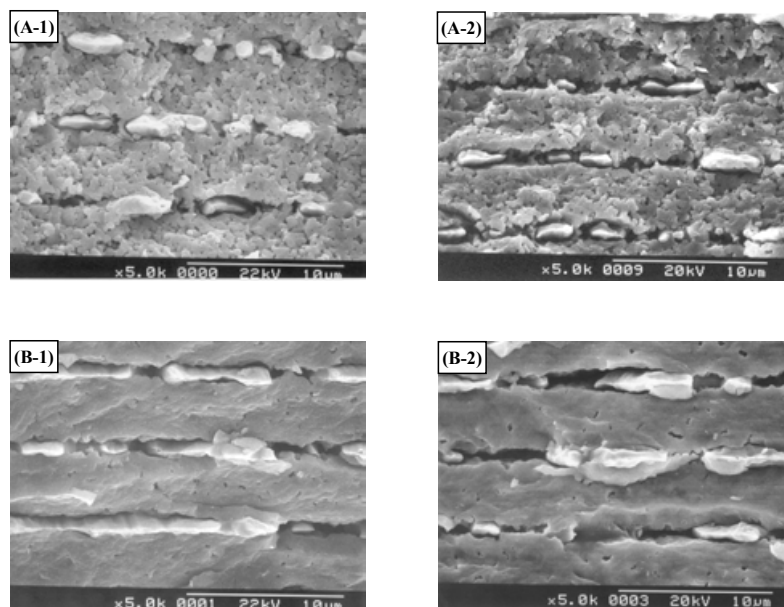


Fig. 6-6 Fracture micrographs of MLCCs with the temperature of (A) 1200°C and (B) 1250°C at the heating rate of 5°C/min in both processes. Numerical series of (1) and (2) in Figs (A) and (B) indicate the holding time of 3h and 6h, respectively.

6.4 Conclusions

The pore size distribution was greatly affected not only by the heating rate in the burnout process, but also by sintering temperature at the same heating rate, showing that the pore size distribution became narrow with a decrease and an increase of the heating rate and sintering temperature, respectively. The heating rate in the burnout process on the pore size distribution, hysteresis, and cumulative pore surface area, was more effective than that in the sintering. The slow heating rate is more effective in removing the residual pores and developing the microstructure. The control of heating rate in the sintering process did not give any effect on the microstructural development, indicating that the heating rate in the burnout process related to the rearrangement of particles have to be controlled as the low heating rate. The pore evolution was rapidly progressed between 1200°C and 1250°C, and the full densification was achieved at 1300°C with the holding time of 3h, in which the holding time restrictively affected the microstructure. Consequently, the slow heating rate in the burnout process and a critical sintering temperature with holding time were required to reach the full densification which was achieved at 1300°C with the holding time of 3h at the heating rate of 1°C/min in the burnout process

Chapter 7. Conclusions

The burnout conditions in multilayer ceramic capacitors (MLCCs) have been investigated to optimize the binder removal and to control the microstructure after the burnout process. Also, the effects of the heating profile in the burnout and sintering processes, especially the heating rate and holding time, on the pore evolution and microstructure in multilayer ceramic capacitors (MLCCs), showing Y5V characteristics, were investigated in order to optimize the fabrication process.

The delamination in MLCCs is created at a faster heating rate in the ambient atmosphere, independent of temperature. However, MLCCs prepared under the reducing atmosphere ($\text{Ar}/\text{H}_2 = 97/3$) do not present any defects such as the delamination and cracks observed in the ambient atmosphere at the heating rate of 7°C . The effects of the temperature and atmosphere in the burnout process on the cumulative pore surface area and microstructure are superior to the heating rate, even though the pore size distribution became narrower and the mean pore size larger with an increase of the heating rate. The burnout process has to be performed at the low temperature in the ambient and at the high temperature in the reducing with slower heating rate.

At heating rates of $1^\circ\text{C}/\text{min}$, $3^\circ\text{C}/\text{min}$, and $5^\circ\text{C}/\text{min}$ in both processes with and without the holding time at the sintering temperature, the pore size distribution became narrow with a decrease and an increase of the heating rate and sintering temperature, respectively, showing no effect

by the heating rate in the sintering process. The results of the hysteresis and cumulative pore surface area are very consistent with the results of the pore size distribution, indicating that the effect of the heating rate in the burnout process was superior to that in the sintering process. The necking between particles was observed at the temperature of 1100°C and pore evolution rapidly progressed between 1100°C and 1200°C. Control of the heating rate in the burnout process was more important than that in the sintering process for pore evolution, even though the heating rate in the sintering process partially affected the final microstructure, indicating that the rearrangement of particles finished during the binder burnout process continued to affect the sintering process. The holding time was also effective in removing the residual pores and in developing the final microstructure.

Consequently, the atmosphere and temperature in the burnout process play a more important role in preventing the defects and in controlling the microstructure in MLCCs than the heating rate, and the heating rate in the burnout process is more important than that in the sintering process. The holding time have to be given to achieve the full densification in the final sintering temperature, but the sintering temperature is more effective in removing the residual pores and developing the microstructure than the holding time.

요 약 문

Tape casting법으로 제조된 MLCCs를 burnout 공정에서 burnout온도, 분위기, heating rate에 따른 pore 구조, 크기와 burnout미세구조의 영향 및 burnout공정과 소결공정에서 heating rate의 profile에 따른 기공진화 및 소결미세구조에 미치는 영향을 고찰하였다.

Burnout공정의 산화분위기에서 MLCCs의 delamination는 200℃의 7℃/min, 250℃와 300℃의 6℃/min의 heating rate에서 얻을 수 있었다. MLCCs의 기공크기분포는 burnout 온도와 heating rate가 증가함에 따라 기공분포가 좁아지며, 축적된 기공표면적은 산화와 환원분위기에서 높은 burnout온도와 heating rate에서 최소값을 얻었다. 특히, 환원분위기에서의 MLCCs는 산화분위기보다 작은 축적된 기공표면적을 얻었다. burnout 공정 후 미세구조는 heating rate보다 분위기와 burnout온도에 의존함을 알 수 있었다.

Heating rate(1℃/min, 3℃/min, 5℃/min)에 의해 소결된 MLCCs의 기공크기분포는 소결온도가 증가함에 따라 점차적으로 좁아지며, 기공진화와 관련된 축적된 기공표면적은 소결온도가 증가함에 따라 최소값을 얻었다. heating rate 변화에 따라 소결된 MLCCs의 미세구조는 느린 heating rate에서 효과적으로 치밀화 되었다. burnout 공정에서 heating rate는 소결공정에서의 heating rate보다 미세구조와 기공진화에 큰 영향을 주었다.

References

1. Dieter Voitzke, Hans-peter Abicht, Mechanistic investigations on the densification behavior of barium titanate ceramics, Solid State Sciences 3 (2001) 417-422.
2. Jae-Ho Jeon, Yoo-Dong Hahn, Hai-Doo Kim, Microstructure and dielectric properties of barium-strontium titanate with a functionally graded structure. J. Euro. Ceram. Soc. 21 (2001) 1653-1656.
3. Y. Park, Y. H. Kim, H. G. Kim, The effect of grain size on dielectric behavior of BaTiO₃ based X7R materials, Mater. Lett. 28 (1996) 101-106.
4. S.-F. Wang, T.C.K. Yang, Y.-R. Wang, Y. Kuromitsu, Effect of glass composition on the densification and dielectric properties of BaTiO₃ ceramics, Ceram. International 27 (2001) 157-162.
5. S.-F. Wang, G.O. Dayton, Dielectric properties of fine grained barium titanate based X7R materials, J. Am. Ceram. Soc. 82 (1999) 2677-2682.
6. Y. Mizuno, Y. Okino, N. Kohzu, H. Chazono, H. Kishi, Influence of the microstructure evolution on electrical properties of multilayer capacitors with Ni electrode, Jpn. J. Appl. Phys. 37 (1998) 5227-5231.
7. Y. Okino, N. Kohzu, Y. Mizuno, M. Honda, H. Chazono, H. Kishi, Effects of the microstructure on dielectric properties for BaTiO₃-based MLC with Ni electrode, Key Engineering Materials

157 (1999) 9–15.

8. H. Chazono, Y. Okino, N. Kohzu, H. Kishi, Effect of Sm and Ho addition on the microstructure and electrical properties in MLCC with Ni internal electrode, *Ceramic Transactions* 97 (1999) 53–64.
9. Y. Mizuno, T. Hagiwara, H. Chazono, H. Kishi, Effect of milling process on core-shell microstructure and electrical properties for BaTiO₃-based Ni-MLCC, *J. Europ. Ceram. Soc.* 21 (2001) 1649–1652.
10. H. Saito, H. Chazono, H. Kishi, N. Yamaoka, X7R multilayer ceramic capacitor with nickel electrode, *Jpn. J. Appl. Phys.* 30 (1991) 2307–2310.
11. I. Burn, Ceramic disk capacitors with base-metal electrodes, *Ceram. Bull.* 57(6) (1978) 600–604.
12. R. Moreno, “The role of slip additives in tape casting technology.2 . Binders and plasticizers.” *Am. Ceram. Soc. Bull.* 71 (1992) 1521–1531.
13. D.J. Shanefield, *Organic additives and ceramic processing*, Kluwer Academic, Dordrecht, The Netherlands, 1996.
14. A.W. Tavernor, H.P.S. Li, A.J. Bell, R. Stevens, “Improved Compaction in Multilayer Capacitor Fabrication” , *J. Euro. Ceram. Soc.* 19 (1999) 1691–1695.
15. “Capacitor” ,the Tech Target network of industry-specific IT Web sites
16. Tyra T. Buczkowski. “Capacitor history” , Faradnet Web sites.
17. “Development and material engineering of multilayer ceramic

capacitor", Hanyang Univ. Ceramic Engineering, Micro Multilayered Ceramics Forming Lab.

18. Lionel M. Levinson. "Electronic ceramics" , (1988) 191-266.
19. "Ceramic capacitors" , Chip Center Web sites
20. Michel W. Barsoum. "Fundamentals of ceramic" (1997)70-71.
21. Y. Sakabe, Dielectric materials for base-metal multilayer ceramic capacitors, Am. Ceram. Soc. Bull. 66 (1987) 1338-1341.
22. T. Nomura, T. Kato, Y. Nagano, The 9th US-Japan Seminar on Dielectric and Piezoelectric Ceramics, 1999, pp. 295-298.
23. J. Yamamatsu, N. Kawano, T. Arashi, A. Sato, Y. Nakano, T. Nomura, Reliability of multilayer ceramic capacitors with nickel electrodes, J. Power Sources 60 (1996) 199-203.
24. D.F.K. Hennings, Dielectric materials for sintering in reducing atmosphere, J. Euro. Ceram. Soc. 21 (2001) 1637-1642.
25. N. Halder, D. Chattopadhyay, A.D. Sharma, D. Saha, A. Sen, H.S. Maiti, Effect of sintering atmosphere on the dielectric properties of barium titanate based capacitors, Mater. Res. Bull. 36 (1991) 905-913.
26. H.T. Kim, J.H. Adair, M.T. Lanagan, Thermomechanical behavior of BME capacitors during binder burnout, Am. Ceram. Soc. Bull. 80(10) (2001) 34-38.
27. N. Das, H.S. Maiti, Formation of pore structure in tape-cast alumina membranes effects of binder content and firing temperature, J. Membrane Sci. 140(1998) 205-212.

28. S. Westermarck, A.M. Juppo, L. Kervinen, J. Yliruusi, Pore structure and surface area of mannitol powder, granules and tablets determined with mercury porosimetry and nitrogen adsorption, *Euro. J. Pharm. Biopharm.* 46 (1998) 61–68.
29. L. Moscou, S. Lub, Practical use of mercury porosimetry in the study of porous solids, *Powder Tech.* 29 (1981) 45–52.
30. F.A.L. Dullien, *Porous media: Fluid transport and pore structure*, 2nd ed., Academic Press, New York, 1992.
31. G.P. Matthews, C.J. Ridgway, M.C. Spearing, Void space modeling of mercury intrusion hysteresis in sandstone, paper coating and other porous media, *J. Colloid Interface Sci.* 171 (1995) 8–27.
32. S. Lowell, J.E. Shields, *Powder surface area and porosity*, 3rd ed., Chapman and Hall, New York, 1991.
33. T. Tsurumi, Y. Yamamoto, N. Ohashi, H. Chazono, Y. Inomata, H. Kishi, *Proceedings of the 9th US–Japan seminar on dielectric and piezoelectric ceramics*, 1999. pp. 345.
34. Y. Sakabe, Dielectric materials for base-metal multilayer ceramic capacitors, *Am. Ceram. Soc. Bull.* 66 (1987) 1338–1341.
35. C. Alie, R. Pirard, J.P. Pirard, Mercury porosimetry applied to porous silica materials: successive buckling and intrusion mechanisms, *Coll. Surf. A* 187–188 (2001) 367–374.
36. H. Chazono, Y. Inomata, N. Kohzu, H. Kishi, *Electroceramics in Japan II*, N. Mizutani, K. Shinozaki, N. Kamhara, T. Kimura, Eds. Trans. Tech. Publications Ltd. CSJ Series Vol. 5, 1999.

37. H. Chazono, Y. Inomata, N. Kohzu, H. Kishi, Electroceramics in Japan III, N. Mizutani, K. Shinozaki, N. Kamhara, T. Kimura, Eds. Trans. Trech. Publications Ltd. CSJ Series Vol. 6, 1999.
38. S. Masia, P. Calvert, W.E. Rhine, H.K. Bowen, Effect of oxides on binder burnout during ceramics processing, J. Mater. Sci. 24 (1989) 1907-1912.
39. M.J. Cima, M. Dudziak, J.A. Lewis, Observation of poly(vinyl-butyril)-dibutyl phthalate binder capillary migration, J. Am. Ceram. Soc. 24 (1989) 1087-1090.
40. K. Hirakata, S. Sato, F. Uchikoba, Y. Kosaka, K. Sawamura, Multilayer capacitors with copper inner electrodes, Ferroelectrics 133 (1992) 139-144.
41. G. de With, Structural integrity of ceramic multilayer capacitor materials and ceramic multilayer capacitors, J. Euro. Ceram. Soc. 12 (1993) 323-336.
42. H. Mostaghaci, R.J. Brook, J. Mater. Sci. 21 (1986) 3575-3580.
43. H.G. Graham, N.M. Tallan, K.S. Mazdiasni, J. Am. Ceram. Soc. 54 (1971) 548-553.
44. H. Mostaghaci, R.J. Brook, Microstructure development and dielectric properties of fast-fired BaTiO₃ ceramics, J. Mater. Sci. 21 (1986) 3575-3580.
45. H.G. Graham, N.M. Yallan, K.S. Mazdiasni, Electrical properties of high-purity polycrystalline titanate, J. Am. Ceram. Soc. 54 (1971) 548-553.

46. H. Cai, Z. Gui, L. Li, Low-sintering composite multilayer ceramic capacitors with X7R specification, *Mater. Sci. Eng. B83* (2001) 137-141.48.
47. D.H. Kim, U. Paik, K.M. Kang, Y.G. Jung, J.H. Kim, Influence of burnout process on pore structure and burnout microstructure in BaTiO₃ based Y5V materials *J. Mater. Process. Tech.* *submitted*.
48. M. Ciftcioglu, D.M. Smith, S.B. Ross, Mercury Porosimetry of Ordered Sphere Compacts: Investigation of Intrusion and Extrusion Pore Size Distributions, *Powder Tech.* 55 (1988) 193-205.
49. L. Shepperd, Progress continues in capacitor technology, *Am. Ceram. Soc. Bull.*,1933, 72(3), 45-47.
50. U. Paik, K.M. Kang, Y.G. Jung, J.H. Kim, "Binder removal and microstructure with burnout conditions in BaTiO₃ based Ni-MLCCs" *Ceram. Inter.* Submitted.
51. K. M. Kang, Y. G. Jung, U. Paik, J. H. Kim, Pore evolution and microstructure with heating profile in BaTiO₃ based Ni-MLCCs with Y5V specification, *Mater. Research. Bull.* *submitted*.
52. Suk-Joong L. Kang, Sintering(densification, grain growth and microstructure), 1997, pp.7
53. E.W. Washburn, *Phys. Rev.*, 17 (1921), 273. (or E.W. Washburn, Note on a method of determining the distribution of pore sizes in a porous material, *Proc. Nat. Acad. Sci. USA* 7 (1921)

115-116.

54. R.E. Mistler and E.R. Twiname, Tape Casting, Am. Ceram. Soc., Westerville, OH, 2000, pp.152-185.
55. D.J. Shanefield, Organic additives and Ceramic Processing, Kluwer Academic, Norwell, MA, 1996, pp. 171-254.